Parametric study of water vapor and water ice particle plumes based on DSMC calculations: Application to the Enceladus geysers

A. Mahieux[a,b,c,*], D.B. Goldstein[a], P.L. Varghese[a], L.M. Trafton[d]

[a] The University of Texas at Austin, Department of Aerospace Engineering and Engineering Mechanics, Austin, TX, USA
[b] Belgian Institute for Space Aeronomy, Brussels, Belgium
[c] Fonds National de la Recherche Scientifique, Brussels, Belgium
[d] The University of Texas at Austin, Department of Astronomy, Austin, TX, USA

A B S T R A C T

The field parameters – number density, velocity components and temperature – for the Enceladus geysers, and possibly similar jets from other bodies, such as Europa, Ceres or comets, are expensive to obtain using physically correct simulation methods, such as the Direct Simulation Monte Carlo (DSMC) approach. It would be very useful to be able to correctly reproduce all the different states that the flow is undergoing while expanding into vacuum, from a high density and collisional state near the surface to free-molecular and collisionless at high altitude without resorting to expensive DSMC simulations in every case. In this work, we consider a two-phase water vapor/grain mixture exiting a circular vent, assuming a uniform radius of the water ice grains, and study how the field parameters can be fitted at an altitude of 10 km, where the flow is collisionless. To do so, we define simple functional forms for each of these fitted parameters, and we study how their coefficients vary as a function of the vent exit parameters, i.e. the vent radius, the water mixture mass flow, the water vapor/water ice mass ratio, the water ice grain radius, the water vapor and water ice exit speed, the vent exit angle and flow temperature. We define polynomial approximations to model these variations. We show that all the vent parameters have nearly-independent influences on the radial profiles at 10 km, except for the water vapor and water ice exit speed, for which we considered cross-correlations. We finally show that the geyser field parameters can be reconstructed using our parametric study for variations of the vent parameters within the range considered here, and in a time frame of a few milliseconds. The results of the parametrizations presented in this study can now be used to propagate the geyser field parameters using computationally inexpensive free molecular/ballistic codes up to higher altitudes. The DSMC results that have been run for this paper are available at an online repository.

1. Introduction

Various instruments on board the CASSINI spacecraft – ISS (Porco et al., 2004), INMS (Kasprzak et al., 1996), CDA (Srama et al., 2004) and UVIS (Esposito et al., 2004) – observed two-phase water outgassing originating from five crevasses located near the Enceladus South pole (Porco et al., 2006; Spencer et al., 2006), where the surface temperature also was recorded to be warmer than the background on this icy moon of Saturn (Howett et al., 2011; Spencer et al., 2006). These water geysers have been extensively studied since their discovery back in 2005, because they offer an unprecedented window into the composition of the interior of Enceladus. The geysers have been inferred to be mainly composed of water vapor and water ice particles, and extend hundreds of kilometers above the surface. Various authors tried to explain their origin, from near-surface explosion of boiling liquid water (Porco et al., 2006), to clathrate decomposition (Kieffer et al., 2006) or evaporation from a underground salty ocean (Porco et al., 2014; Postberg et al., 2009; Schmidt et al., 2008b), as well as how fluids move up the conduits (Kite and Rubin, 2016).

From these observations, studies have tried to constrain the outgassing flow rate from the observed geysers (Burger et al., 2007; Dong et al., 2011; Hansen et al., 2006; Hansen et al., 2008; Hansen et al., 2011; Saur et al., 2008; Smith et al., 2010; Tenishev et al., 2010; Tenishev et al., 2014; Tian et al., 2007; Waite et al., 2006; Yeoh et al., 2015; Yeoh et al., 2017), together with the flow characteristics, such as its temperature and speed.

The Enceladus plume has been studied using different approaches such as (1) models using ballistic geysers but which ignore the fact the outflowing gas is not collisionless in the very-near-field close to the vent (Dong et al., 2011); (2) assuming analytic solutions to the plume density fields (Teolis et al., 2017); and (3) simple Direct Simulation Monte Carlo (DSMC) approaches (Hedman et al., 2018; Portyankina et al., 2016).

In this work, we present results from a set of single geyser DSMC simulations expanding into vacuum, from which we parametrized the geysers' characteristics at an altitude of 10 km above ground once the flow has becomes collisionless, i.e. considering the two-phase number density, velocity, kinetic and rotational temperature distributions.

* Corresponding author at: The University of Texas at Austin, Department of Aerospace Engineering and Engineering Mechanics, Austin, TX, USA.
E-mail address: arnaud.mahieux@utexas.edu (A. Mahieux).

Table 1

Vent characteristics for the default case. All the values are given for the particles at the surface, as they exit the vent. The mass flow value corresponds to the whole vent.

Vent radius [m]	Mass flow [kg/s]	Water vapor mean speed [m/s]	Water grains mean speed [m/s]	Ice grains mass ratio [%]	Ice grain radius [μm]	Common mixture temperature [K]	Vent exit angle [°]
r_{vent}	$\dot{m}_{total}$	$v_{gas, ini}$	$v_{ice, ini}$	f_{ice}	r_{ice}	T_{ini}	α_v
1.4	13.37×10^{-3}	902	902	5	1	53	0

DSMC simulations are relatively computationally expensive, with a computation time larger than 48 h using four processors for a single adequately resolved geyser calculation, suggesting that this approach would be too time consuming for direct non-linear fitting of the far-field flow from multiple geysers with the source parameters of each varied independently. However, the parametrizations presented in this work can now be used to quickly, i.e. in a few ms, and robustly reconstruct the plume characteristics at 10 km above the surface, considering variations of the outgassing flow characteristics at the vent, such as the vent radius, the mass flow, the water vapor/water ice particle mass ratio, the water vapor and water ice speed, the vent exit opening angle, the water ice particle radius and the flow temperature. Note that our parametric study does not need to assume anything specific about details of the flow below ground as we only start simulations at ground level. These parametrizations can then be used to calculate the flow properties at altitudes larger than 10 km, using a computationally cheap free-molecular code, since the flow is reliably non-collisional at these altitudes.

In the near future, we will pursue this higher altitude work, to extend previous studies in our group (Yeoh et al., 2015; Yeoh et al., 2017), and use these parametric results to fit and constrain the measurements from the various CASSINI instruments of the Enceladus South pole two-phased water plumes. However, the work presented here has broader applications. We aim to provide the community with careful and reliable parametrizations, that can be used to reproduce the far-field of the Enceladus water plumes, without having to recompute the expensive DSMC simulations. Beyond Enceladus, our parametric fits are applicable to study the similar plumes thought to exist on Europa (Berg, 2015; Quick et al., 2013), on comets or on any airless body as long as (1) the situations remains within the range of this parametric study and (2) gravity has not begun to dominate the gas dynamics. In fact, the results presented here even have engineering applications to issues of spacecraft contamination by rocket plumes (Dettleff, 1991).

2. DSMC model

2.1. General presentation

We model the near-field of the outgassing geysers using the PLANET DSMC code (Bird, 1994; Yeoh et al., 2015), from the surface of Enceladus up to an altitude of 10 km from the center of the vent. A DSMC approach is suitable for the simulation of this problem since it can model all the different states that the flow is undergoing while expanding into vacuum, from a high density and collisional configuration at the surface to free-molecular and collisionless at high altitude. The mass flow $\dot{m}_{total}$ is composed of a water vapor flow $\dot{m}_{H_2O}$ and water ice particle flow $\dot{m}_{ice}$. The grains are considered to have a uniform radius r_{ice}, with a mass fraction of ice particles $f_{ice} = \frac{\dot{m}_{ice}}{\dot{m}_{H_2O} + \dot{m}_{ice}}$. The gas and ice flow exits the vent with a speed $v_{gas, ini}$ and $v_{ice, ini}$ respectively, and at an common temperature T_{ini}, i.e. $T_{ini} = T_{kin,gas} = T_{rot,gas} = T_{kin,ice} = T_{thermal,ice}$, where $T_{kin, gas}$ and $T_{rot, gas}$ are the kinetic and rotational temperature of the water vapor, respectively, and $T_{kin, ice}$ and $T_{thermal, ice}$ are the kinetic and thermal temperature of the ice particles. The ice density is taken as 921 kg/m^3. Because of the cold temperatures at Enceladus (~ 50 K), we assume vibrations of water molecules are not excited and neglect related radiative transfer processes.

We note here that we made some simplifications regarding the characteristics of the outflowing water mixture. First, we only consider ice particles of uniform radius in this work. A more realistic simulation would consider ice particle size distributions. The uniform radius can be regarded as the mean particle size and the effect of particle size distributions will be considered in future work. Second, we imposed equal kinetic temperature at the vent for both water phases, which is not the most general case for the vent flow. Some studies show the water ice grains might have larger kinetic temperature than the water vapor (Schmidt et al., 2008b).

The water vapor and ice particles are inserted in the domain at the vent located at the surface of the moon, with an imposed mean velocity, thermal velocity and rotational temperature. Based on the studies of Yeoh et al. (2017), we define our default simulation case with the parameters listed in Table 1. Hence, this paper is the follow-up of the work initiated by Yeoh et al. (2015, 2017), where the reader can find all physical details and justifications about the choice of the default case simulation. Thus, we only review the most important information from these previous studies. These values are derived considering a source of water located below ground at triple point conditions (Schmidt et al., 2008b), which is assumed to expand adiabatically in the underground nozzle up to the vent hole at the surface. In this case, the speeds of both water vapor particles and ice particles are equal, and correspond to Mach 5 conditions – relative to the water vapor alone, the speed of sound of the pure vapor in these conditions is equal to $\sqrt{\gamma R T_{ini}} = 180.4$ m/s, with $\gamma = \frac{4}{3}$. In the default case, the velocity vectors are normal to the planet surface. The simulation does not account for planetary rotation effects – i.e. Coriolis and centrifugal forces, since these have negligible effects for the altitude range considered here (Yeoh et al., 2015).

Even though the PLANET code allows consideration of these mechanisms, sublimation of the ice particles and condensation of the gas are not considered in the present DSMC simulations, as justified in Yeoh et al. (2015). Also, as already mentioned, H$_2$O infrared vibrational/rotational cooling of the gas is not turned on in the DSMC calculations.

In the DSMC approach in general, both gas molecules, which are modeled using the variable hard sphere model (Bird, 1994), and particles can collide and exchange energy, i.e. molecule-molecule and molecule- particle interactions are considered. Collisions between ice particles are neglected because they rarely occur – see Section 2.3 for justification. We assume that gas molecules collide with ice particles with pure diffuse reflection, which allows the transfer of momentum, kinetic and internal energy. The water vapor molecules have three rotational degrees of freedom that can be excited during collision with other molecules, using the Larsen-Borgnakke energy exchange model (Bird, 1994). The ice particles have no rotational degrees of freedom – as they are assumed to have negligible rotational kinetic energy about heir centers of mass, but they possess an internal thermal temperature. To calculate the probability of the collisions between particles, we define a grid of collision "cells", in which collision probabilities and outcomes are calculated. In order to resolve the molecular collision time – MCT, the average time between two successive collisions of a molecule – and the mean free path – MFP, the mean distance between these collisions – of the outflowing molecules and particles, we perform the DSMC calculation in eight nested stages. Each stage corresponds to
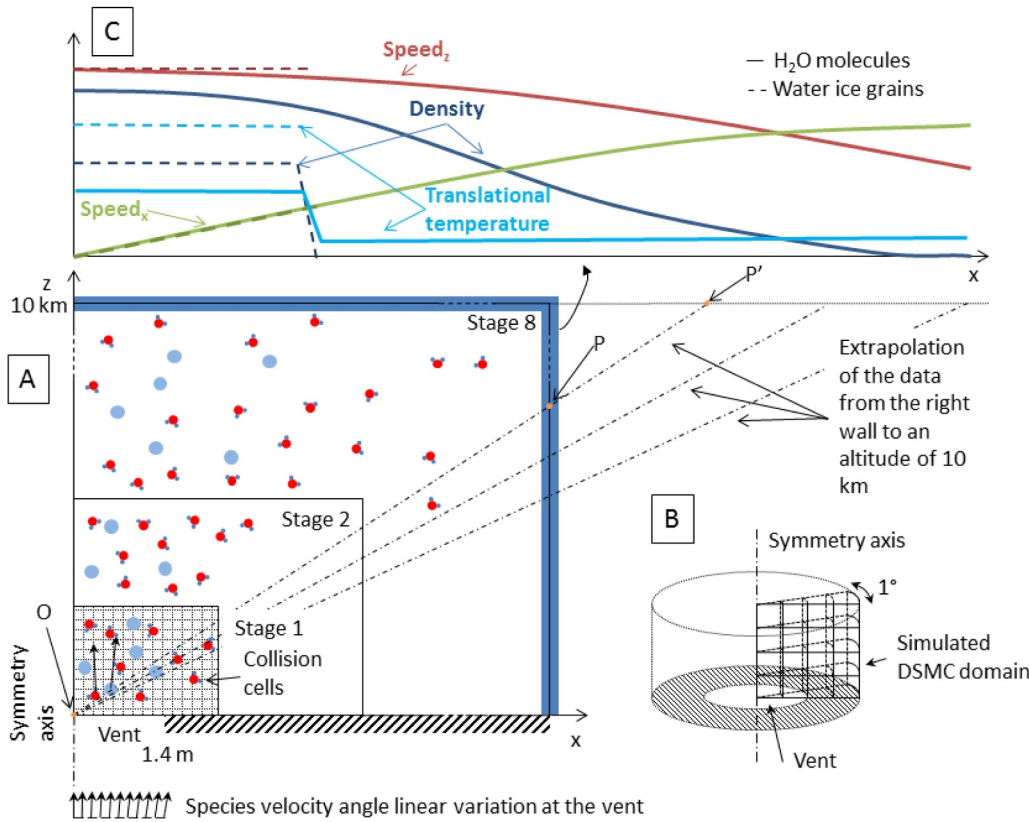
Fig. 1. Panel A: Schematic of the DSMC domain in 2D, x is the radial direction and z is the vertical direction, where the radial and vertical directions refer to the local cylindrical coordinates attached to the geyser vent. The z-axis is the axis of symmetry. The stages are depicted by the black boxes. The collision cells are shown only in stage 1 for clarity. The distribution of velocity vectors at the vent are shown at the bottom of the figure. The points O, P and P', together with the dashed lines starting from the center of the vent, crossing the right wall of stage 8 (geometric stages 3 to 7 not shown) and the 10 km altitude boundary, depict the geometry of the correction process used in the parametrization of Section 3. Panel B: 3D schematic of the cell structure near the vent. Panel C: Number density, vertical and radial speed components and the kinetic temperature radial profiles at 10 km of water vapor and water ice particles.

Table 2
Comparisons between the cell size and the MFP and between the simulation time step and the MCT for each stage of the default simulation case. The MFP and MCT are averaged over the whole stage domain. The ratio between the real and simulated particles, f_{num}, is also given for large radial values.

Stage number	Cell width[m]	Cell height[m]	Mean MFP [m]	Time step [s]	Mean MCT [s]	f_{num} for $x \to \infty$
1	0.004	0.004	0.002	9×10^{-7}	3.8×10^{-6}	6×10^{13}
2	0.010	0.014	0.009	3×10^{-6}	1.6×10^{-5}	3.9×10^{14}
3	0.042	0.024	0.052	7×10^{-6}	9×10^{-5}	2×10^{15}
4	0.074	0.144	0.575	3×10^{-5}	9.7×10^{-4}	1.3×10^{16}
5	0.244	0.484	6.919	8×10^{-5}	1.1×10^{-2}	8×10^{16}
6	0.830	1.654	81.45	3×10^{-4}	0.13	5×10^{17}
7	2.862	5.718	955.5	1×10^{-3}	1.53	3.2×10^{18}
8	20	20	17,783.6	4×10^{-3}	30.1	2.1×10^{19}

an increasing fraction of the spatial domain, encompassing the previous one, see Panel A of schematic Fig. 1, and with sizes following geometric progressions. In each stage, we define a simulation time step such that it is smaller than the MCT, and a length of the cells to be ideally smaller than the local MFP. The staging procedure is described in detail in Yeoh et al. (2015). Similar to what was done by Berg et al. (2016) for the Europa plumes, we use a large number of cells to correctly represent molecular collisions, and thus correctly resolve spatial gradients in the simulation. In each stage, the number of cells in the horizontal and vertical directions is equal to 500, in order to resolve the MFP. The MFP is very small at the vent, and becomes geometrically larger with altitude. This multi-stage method can be used because the gas flow is supersonic, which means that no material is returning from an upper stage to a lower stage. Table 2 summarizes, for the default case conditions described in Table 1, the size of the collision cells and the MFP for the eight stages, together with the time step in each stage and the corresponding MCT. The time step always resolves the MCT, while the cell size only fully resolves the MFP for stages larger than two. However, sensitivity tests run by Yeoh et al. (2015) showed than this does not affect the solution since the gas is well into the continuum regime in stages 1 and 2. We conducted a sensitivity study of the number of cells

in the horizontal and vertical directions, i.e. the effect of spatial resolution, similar to what was done in Yeoh et al., (2015). We too conclude that the computed density, temperature and velocity component fields are independent of the spatial resolution within the random noise, considering the number of cells used in this work.

Since our DSMC code PLANET uses spherical coordinates, we consider one cell in the azimuthal direction, which has a 1° size. As a consequence, a singularity occurs at the symmetry axis, and the volume of the cells increases with larger radial coordinate. To ensure a sufficient number of numerical particles close to the symmetry axis, we use a non-uniform weighting f_{num} in the horizontal direction, where f_{num} is the ratio between real and simulated particles in the DSMC simulation. It is linearly decreased by a factor 100 from the symmetry axis up to a distance of 2 km.

The simulations are run for a long enough time so that all the physical parameters – number density, speed and temperature – reach a steady state in each stage, before the calculation proceeds to sample data at the top of a stage and pass it on the next stage; hence the simulation time length can be estimated based on the height of a stage and on the flow speed at the base of the stage. In this work we only consider the steady state of the geyser fields.
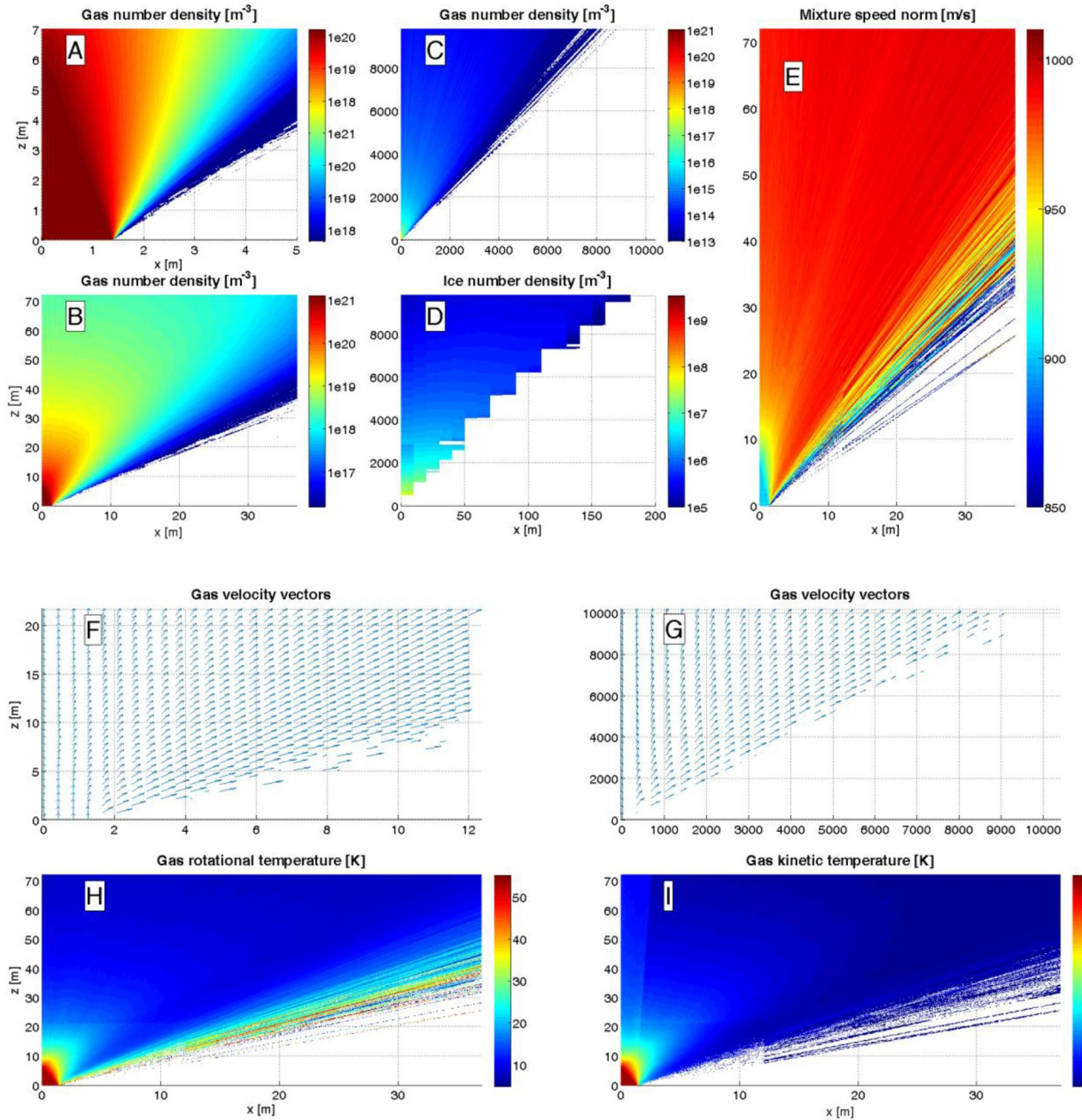
Fig. 2. Panels A to C: H$_2$O molecule number density in [m^{-3}], at the vent up to stage 1 in Panel A, close to the vent up to stage 4 in Panel B, for the whole domain up to stage 8 in Panel C. Panel D: Ice particle number density for the whole domain in [m^{-3}], up to stage 8. Panel E: speed of water vapor and ice particle mixture in [m/ s], up to stage 4. Panels F and G: Velocity vectors close to the vent in Panel F, up to stage 3, and for the whole domain in Panel G, up to stage 8. Panels H and I: H$_2$O rotational and kinetic temperature close to the vent in [K], up to stage 4.

2.2. Default case results

The results for the default case are presented in Fig. 2. The density field close to the vent is shown in Panels A and B (up to 7 m and 70 m of altitude), where the expansion wave is clearly seen in Panel A as it originates from the edge of the vent and intersects the symmetry axis at a height of $h_{exp} = \frac{r_{vent}}{\tan \mu} = r_{vent} \cdot \sqrt{M_{exit}^2 - 1} = 6.86$ m, with μ the Mach angle, defined as $\sin \mu = \frac{1}{M_{exit}}$, which is the angle between the symmetry axis and the expansion wave – see Eq. (9.1) page 606 in Anderson (2011) for example. The complete density field is shown in Panel C – note the change in color bar. At an altitude of 10 km, the upper boundary of this simulation, the geyser extends out to ~8 km in the radial direction. Panel D shows the ice particle density field. One

can see that the grains, which are individually much more massive than the gas molecules, remain close to the symmetry axis: the radius of the ice particle cone is equal to only ~200 m at 10 km. Due to their large mass, the grains follow a nearly ballistic trajectory as they exit the vent. Their non-zero kinetic temperature reflects the dispersion in grain velocities, of the order of a few cm/s, which results in a non-zero spreading angle of the ice cone as the plume expands into space even if vent conditions give negligible gas drag. Note that velocity differences of a few cm/s at the vent are sufficient to spread the ice particles over a cone radius of O(10 m) at 10 km altitude. Additionally, the grains are moved away from the symmetry axis by gas drag induced by collisions with the water vapor, which induces a non-zero radial speed and further enlarges the ice particle cone as it gains altitude. The flow speed

Table 3

List of the functional forms used to fit the physical parameters listed in the first column. x represents the radial distance.

Variable	Water vapor	Ice grains
Plume width, W_{gas}	$\log_{10}(W_{gas}) = j_0$	$\log_{10}(W_{ice}) = k_0$
Number density, n_{gas}	$\log_{10}(n_{gas}) = a_0 + a_2 \cdot (\frac{x}{W_{gas}})^2 + a_3 \cdot (\frac{x}{W_{gas}})^3$	$\log_{10}(n_{ice}) = (b_0 + b_1 \cdot x) \cdot (1 - \tanh(100 \cdot (x - b_2)))$
Vertical speed, v_{gas}	$\log_{10}(v_{gas}) = $ $c_0 \cdot \cos(c_1 \cdot x + c_2 \cdot x^2)$	$\log_{10}(v_{ice}) = d_0 + d_2 \cdot (\frac{x}{W_{ice}})^2$
Radial speed, u_{gas}	$u_{gas} = e_0 \cdot \sin(e_1 \cdot x) + e_2$	$u_{ice} = f_0 + f_1 \cdot x$
Rotational temperature, $T_{rot, gas}$	$\log_{10}(T_{rot, gas}) = g_0 + g_2 \cdot x^2$	
Kinetic temperature, $T_{kin, gas}$	$T_{kin,gas} = h_0$ $+ h_1 \cdot (1 - \tanh(100 \cdot (x - h_2)))$	$T_{kin,ice} = i_0$

field of both gas molecules and ice particles is shown in Panel E. The mixture expansion into vacuum is clearly seen in the first 10 m above the vent, where it accelerates from 902 m/s to ~1000 m/s at altitudes larger than 60 m. The unit normalized vector velocity field is shown in Panel F close to the vent and Panel G for the whole simulation domain. As the gas expands into vacuum, the gas molecules are expanding in the radial direction, tilting the velocity vectors. As noted above, this induces a radial drag force on the ice particles that helps to move them away from the symmetry axis. Finally, the rotational and kinetic temperature fields are depicted for the region close to the vent in Panels H and I, respectively. In Panel G, the rotational temperature decreases with altitude because of dynamic gas expansion. In Panel I, the same effect is observed for the kinetic temperature, except in the region close to the symmetry axis, where the gas remains warmer because of the presence of the water ice particles. The ice particle local number density remains high at all altitudes, and collisions between ice particles and water vapor remain frequent. Thus, the ice particles raise the kinetic temperature of the water vapor in the region close to the symmetry axis.

2.3. Gradient local Knudsen number

We examine the values of the gradient local Knudsen number in order to check if the flow is non-collisional at an altitude of 10 km. We define the gradient local Knudsen number, Kn_{grad}, as the ratio between the local MFP and the scale length of the macroscopic flow property gradient, which is chosen in the present case to be the ratio between the water vapor number density and the norm of its spatial gradient. Hence

$$Kn_{grad, gas} = \lambda_{MFP, gas} \cdot \frac{\nabla m_{gas}}{m_{gas}} \quad (1)$$

with λ_{MFP} the MFP and m_{gas} the water vapor number density field. For the default simulation case, the Knudsen number varies approximately exponentially between $Kn_{grad, gas}(x = 0 \text{ km}, z = 10 \text{ km}) \approx 10$ and $Kn_{grad, gas}(x = 8 \text{ km}, z = 10 \text{ km}) \approx 10^5$ along the edge of the geyser. In the continuum regime (strongly collisional) $Kn_{grad} \ll 1$, and the flow is free molecular if $Kn_{grad} \gg 1$. Based on this DSMC simulation we can conclude that the flow is free molecular at 10 km of altitude. Similarly, we evaluate the Knudsen number for the ice particles at 1 m above the vent and at 10 km, $Kn_{grad, ice}(x = 0 \text{ m}, z = 1 \text{ m}) \approx$ $Kn_{grad, ice}(x = 1.4 \text{ m}, z = 1 \text{ m}) \approx 10$, $Kn_{grad, ice}(x = 0 \text{ m}, z = 10 \text{ km}) \approx 100$ and $Kn_{grad, ice}(x = 150 \text{ m}, z = 10 \text{ km}) \approx 10^6$. The ice particle flow is thus non-collisional at any altitude of the simulation. This justifies the assumption that collisions between ice particles are negligible that was noted in Section 2.1.

3. Parametrization of the radial profiles

3.1. Extrapolation of the radial profile

In the following section, we are interested in the flow parameters at

the 10 km altitude upper boundary of the domain, which we term radial profiles, and building their parametrizations using functional forms. However, since the DSMC domain is nearly rectangular in the vertical-radial directions, if it is spread broadly enough, the geyser at 10 km might also cross the right wall of the domain, see Fig. 1. Let us consider a point, P, on the right wall. We define the projection of this point on the 10 km altitude boundary P' as seen from the center of the vent O, and we extrapolate the number density value by multiplying it by the distance ratio $(\frac{\|OP\|}{\|OP'\|})^3$, where $\|OP\|$ denotes the distance between the center of the vent and the point P. The third power of the distance ratio is considered here since we can assume (1) a roughly hemispherical expansion from the vent center treated as a point source when sufficiently far away (2) the flow is collisionless at this distance from the vent, as explained in the previous section, i.e. that the gradient local Knudsen number is much larger than 1. Both conditions are met in the present case. The geometry of this operation is depicted in Fig. 1, and its validity was tested on simulations. Note that this extrapolation is rarely employed – it is not needed in the default case, see Panel C of Fig. 2, because the default size of the domain is such that the flow field only crosses its top boundary. Broader spread of the flow in the radial direction is only observed when there is a large velocity slip between the water vapor and ice grains, as will be shown in the next sections.

3.2. Functional forms definition

For each physical quantity of each species, we defined a functional form used for the parametric fit at the 10 km radial extracted slice, based, when possible, on physical and previous work (Dettleff, 1991; Draper and Hill, 1966), or on a best-fit approach in the other cases. In the second case, we choose the functional forms to give the best possible fit to the radial profiles at 10 km, while minimizing the number of coefficients required for the fit. For this reason, some coefficients are set to zero, to account for the axial symmetry of the problem. These functions are listed in Table 3. The fits are obtained using a standard Levenberg-Marquardt algorithm from MATLAB, weighting the data inversely by the numerical noise level from the simulation, assuming a Poisson distribution among the numerical particles, i.e. that the numerical noise level is inversely proportional to the square root of the number of numerical particles in a cell. The fitting algorithm returns the coefficients of the functional form fits, together with their associated uncertainties.

The fits are chosen as follows:

a The water vapor number density n_{gas} is fitted as the decimal power of a third order polynomial, with the radial distance normalized by the width of the geyser at 10 km, W_{gas}. The first-order coefficient a_1 is set to zero for symmetry reasons, i.e. to ensure that $\frac{\partial n_{gas}}{\partial x}|_{x=0 \text{ km}, z=10 \text{ km}} = 0$. We used a modified version of the expression from Draper and Hill (1966), who, from an exact methods of characteristics solution of a nozzle flow expanding into vacuum, proposed to model the number density as $n_{gas} = \frac{B}{r^2} \cdot \exp(-\kappa \cdot (1 - \cos\theta)^2)$, where B
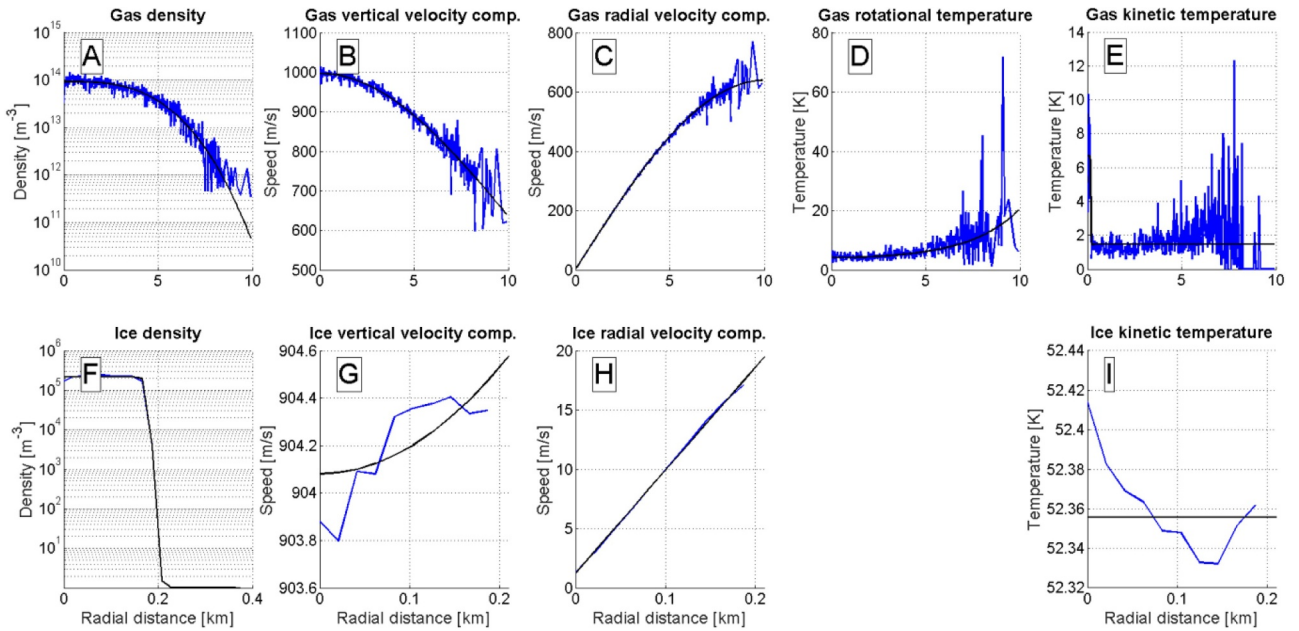
Fig. 3. Number density (Panels A and F in [m^{-3}]), vertical component of the velocity (Panels B and G in [m/s]), radial component of the velocity (Panels C and H in [m/s]), rotational temperature (Panel D in [K]) and kinetic temperature (Panel E and I in [K]) of water vapor (Panels A–E) and ice particles (Panels F to I) radial profiles at an altitude of 10 km for the DSMC simulation of the default case. The blue curves are the DSMC results while the black curves are the best fits using the functional forms described in Table 3. The RMS and noise levels are summarized in Table 4. (For interpretation of the references to color in this figure legend, the reader is referred to the web version of this article.)

and κ are constants, r is the distance to the nozzle, constant in our case, and θ is the angle from the flow symmetry axis in the radial-vertical plane; it is related to our x variable by the relation $x\,[km] = 10 \cdot \cos(\theta)$. Here, we used a third order polynomial expansion of the $(1 - \cos\theta)^2$ term, using the radial distance x as variable, motivated by the fact that this gives a good fit to the DSMC density radial profiles.

b The vertical speed v_{gas} is fitted as the decimal power of a cosine, whose argument is a second-order polynomial without a constant term to ensure that the maximum of the curve is at the symmetry axis. This expression is derived from the work of Dettleff (1991), who gives an expression similar to the one presented here, but as a function of the angle θ defined above.

c The radial speed u_{gas} is fitted as the sum of a sine and a constant value, as they are the first two first terms from a Fourier series expansion.

d The rotational temperature $T_{rot,\ gas}$ is fitted as the decimal power of a parabola, with no first-order coefficient g_1. This expression is chosen by numerical considerations, as it is the one that best fits the DSMC rotational temperature radial profiles.

e The kinetic temperature $T_{kin,\ gas}$ has a rather complicated chosen functional form, in order to correctly reproduce the temperature difference between the radial region where ice particles are present or not. We chose to fit $T_{kin,\ gas}$ as the sum of a constant h_0, which fits the region where no ice particles are present, by the complement of the hyperbolic tangent of a first-order polynomial, covering the region where ice particles are present, multiplied by a high number – 100 – which ensures a steep slope between the two regions, as observed in the data. One parameter, h_1, governs the temperature which is assumed to be uniform close to the symmetry axis, while the parameter h_2 represents the radial value at which the temperature goes from one regime to another. This expression is also chosen for numerical considerations, as it the most simple form we found to reproduce the rather complicate radial profile, that needs to correctly reproduce the larger temperatures observed within the ice

grain core, and cooler on the edges of the geyser.

f The geyser width at 10 km W_{gas} is fitted by the decimal power of a single number. The width of the plume is determined based on the largest x corresponding to a non-zero water vapor number density value, with the condition that all lower x values must have a non-zero water vapor number density.

g For the ice particles, the decimal logarithm of the number density n_{ice} is fitted using a hyperbolic tangent function, which simulates the cut-off radial value where no more ice is present through the parameter b_2, the whole expression being multiplied by a linear variation of the number density decimal logarithm. This rather complicated expression was chosen to correctly reproduce the sudden drop of the radial ice particle number density profile at the edge of the ice particles cone. Based on numerical tests, a linear variation of the number density as a function of the radial distance within the ice grain cone, turns to be precise enough to model the radial variations.

h The decimal logarithm of the vertical speed v_{ice} is fitted as a parabola without a first-order term d_1, while the radial distance is normalized by the width of the ice particles cone at 10 km, W_{ice}. This expression was chosen based on numerical considerations, in order to best fit the DSMC interpolations at 10 km; the use of a decimal logarithm is motivated by the corresponding expression of the water vapor vertical speed.

i The radial speed u_{ice} is fitted as a first-order polynomial, chosen based on the observed shape of the radial speed profiles obtained from the DSMC simulation.

j The kinetic temperature $T_{kin,\ ice}$ is fitted as a constant as we do not expect the ice particle kinetic temperature to change within the ice cone. Collisions between water ice grains and water vapor only weakly affect the ice grains as the mixture expands into vacuum, due to the large mass difference between the water vapor and ice grains.

k The ice particles cone width W_{ice} is fitted by the decimal power of a single number. The same criterion as for the determination of W_{gas} is

Table 4

Weighted root mean square (RMS) and weighted noise level for the interpolations of the simulations plotted in Fig. 3. The weights are the number of numerical particles in the cells, see Eqs. (3) and (4).

RMS fit / Noise	Number density [log10(m^{-3})]	Vertical comp. velocity [log10(m/s)]	Radial comp. velocity [m/s]	Rotational temperature [log10(K)]	Kinetic temperature [K]
Water vapor	0.063/0.048	0.004/0.003	0.189/0.041	0.059/0.043	0.316/0.441
Ice grains	0.024/0.109	3·10^{-5}/10^{-5}	0.025/0.181		0.00134/0.064

used.

3.3. Radial profiles at 10 km

The quality of the radial profiles fits for the default simulation case can be seen by looking at Fig. 3, where the DSMC results are given as the blue curves and the best fits as the black curves. For each fit, the weighted root mean squares (RMS), and the weighted noise of the radial profiles, are summarized in Table 4. We define

$$RMS = \sqrt{\frac{\sum_{i=1}^{N} [(y_{i,DSMC} - y_{i,fit})^2 \cdot y_{i,num}]}{(N - n_{coeff}) \cdot \sum_{i=1}^{N} [y_{i,num}]}} \qquad (2)$$

where i is the running radial index, varying from 0 to N, the number of sampling points, $y_{i,\,DSMC}$ is the variable value from the DSMC interpolation at radial distance $x = x_i$, $y_{i,\,fit}$ is the value from the functional form fit at x_i, $y_{i,\,num}$ is the number of numerical particles at that same radial distance and n_{coeff} is the number of coefficients used in the functional form fit. The decimal logarithm of the concerned variable is taken on $y_{i,\,DSMC}$ and $y_{i,\,fit}$ if it is considered in the fit, see Table 3. For the weighted noise, we use a high pass Fast Fourier Transform filter to remove the low frequency variation of the concerned variable and define this quantity as $\breve{y}_i$, and we have

$$\sigma_y = \sqrt{\frac{\sum_{i=1}^{N} [\breve{y}^2_{i,DSMC} \cdot \breve{y}_{i,num}]}{N \cdot \sum_{i=1}^{N} [\breve{y}_{i,num}]}} \qquad (3)$$

Again, the decimal logarithm of y_i is considered if it is taken in Table 3. The weighted noise is used here in comparison with the RMS to evaluate the quality of the parametrizations.

From Fig. 3, we see that, for water vapor, the number density is decreasing exponentially with increasing radius, while the vertical speed is decreasing quadratically and the radial speed increasing nearly linearly; the speed norm, however, remains nearly uniform with a value of ~1000 m/s. The rotational temperature is very low and is increasing slightly with the radial distance. The kinetic temperature is larger in the radial region where the ice particles are present: 7 K compared to 1.5 K outside of the ice grain cone. Hence, as described above, the presence of the grains sustains the gas kinetic temperature, which is correctly captured by the functional form chosen. For the ice particles, the number density is nearly uniform until it drops to zero at the edge of the ice particle cone. The vertical speed is also nearly uniform, while the radial speed increases linearly with increasing radius. Finally, the grain kinetic temperature is also nearly uniform. In Table 4, all the RMS values are of the same order of magnitude as the noise, validating the qualitative appeal of the fits using the functional forms presented in Table 3.

4. Variation of the vent parameters

4.1. Linearization process description

We defined default values for the vent parameters in the previous section. Here, we will vary these parameters, and study how these variations affect the functional fits at 10 km altitude, by examining how the coefficients of the functional forms given in Table 3 vary with the vent parameters. This can be expressed as follows: let us consider a functional form $\mathcal{F}(x; \xi_k)$, with x the radial distance, and ξ_k the list or collection of coefficients of the functional form as listed in Table 3. For example, if we consider the functional form describing the water vapor radial number density profile $\log_{10}(n_{gas}) = a_0 + a_2 \cdot (\frac{x}{W_{gas}})^2 + a_3 \cdot (\frac{x}{W_{gas}})^3$, ξ_k simultaneously represents a_0, a_2 and a_3.

We thus define $\xi_k = \xi_k(r_{vent}, f_{\dot{m}}, v_{gas,0}, v_{ice,\,0}, r_{ice}, f_{ice}, \alpha_v, T_0)$, with all the variables defined in Table 1. $f_{\dot{m}}$ is a scaling factor for the default mass flow $\dot{m}_{total}$. More generally, we can write $\xi_k = \xi_k(\eta_j)$, with η_j representing one of these vent parameters. The goal is to reconstruct a first-order approximation of the type

$$\mathcal{F}(x; \xi_k(\hat{\eta}_j)) = \mathcal{F}(x; \xi_k(\eta_{j,0})) + \sum_j \frac{\partial \mathcal{F}(x; \xi_k)}{\partial \xi_k} \cdot \frac{\partial \xi_k}{\partial \eta_j} \qquad (4)$$

with $\eta_{j,\,0}$ the default value of the vent parameters and $\hat{\eta}_j$ is a set of vent parameters. To evaluate $\frac{\partial \mathcal{F}(x; \xi_k)}{\partial \xi_k}$, we vary one of the parameters listed in Table 1 at a time, leaving the other parameters unchanged. The ranges of the varied values of each parameter are summarized in Table 6. We chose the range of vent initial conditions based on what is available in the literature – initial speed (Yeoh et al., 2015; Yeoh et al., 2017), grain size (Postberg et al., 2009; Schmidt et al., 2008a), mass outflow (Hansen et al., 2011; Teolis et al., 2010; Yeoh et al., 2015; Yeoh et al., 2017), temperature (Goguen et al., 2013; Spencer et al., 2006), water vapor/water ice ratio (Ingersoll and Ewald, 2011) – and plausible values when it was not available or badly constrained in the literature – vent speed angle and vent radius.

In our study, we assume that all the vent parameters listed above, except for the water vapor and ice grain initial velocities – see lower in the text for explanations, are nearly linearly independent of each other, in the sense that the second-order derivatives $\frac{\partial^2 \xi_k}{\partial \eta_j \cdot \partial \eta_l}$ are assumed to be negligible. This assumption is only partially valid, since some of the vent parameters listed in Table 1 may be intrinsically linked together, by thermodynamical laws for example. However, as a first-order approximation, we assume here that each parameter only influences the others weakly, and that underground conditions can support a combination of vent parameters, and thus are not necessarily in thermodynamic equilibrium. Also, we do not look to constrain the geyser underground conditions that lead to the geyser parameters considered here: this is beyond the scope of this paper and will be addressed in future work; some aspects of the underground conditions were described in Yeoh et al. (2015).

4.2. Water vapor and water ice initial velocities

Our simulations showed that the parametric linear independence assumption described above is not valid for the gas molecule and ice particle mean initial speeds $v_{gas,\,ini}$ and $v_{ice,\,ini}$. That is, having a different initial speed for the water vapor and the ice particles introduces large non-linearity in the geyser flow fields close to the vent, and the effect extends up to 10 km of altitude. This is illustrated in Fig. 4, where we compare the near-field of the geysers for two different situations, with (Case A) water vapor and ice particle speeds equal to 271 and 1082 m/s, respectively (Panels A to D), and (Case B) where the speeds are reversed and equal to 1082 and 271 m/s (Panels E–H), respectively. We note that Case A is extremely improbable, since we do not anticipate underground conditions that would support water ice to exit the geyser
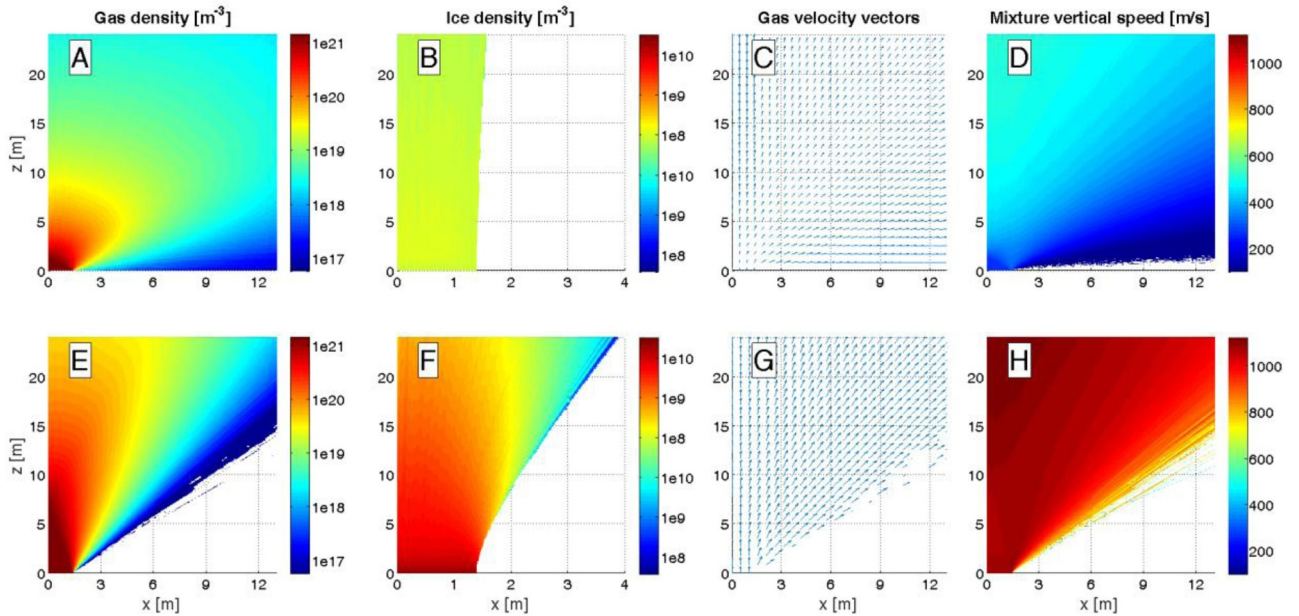
Fig. 4. Comparison between two vent parameter cases, close to the vent, on the first row (Panels A to D) the initial speed of the water vapor is equal to 271 m/s and the ice particles have a speed of 1082 m/s, while on the second row (Panels E–H) the water vapor has a speed of 1082 m/s and the ice particles of 271 m/s. Panels A and E show the water vapor number density in $[m^{-3}]$, Panels B and F the ice particle number density in $[m^{-3}]$, Panels C and G depict the gas velocity vectors and finally Panels D and H show the vertical component of the speed.
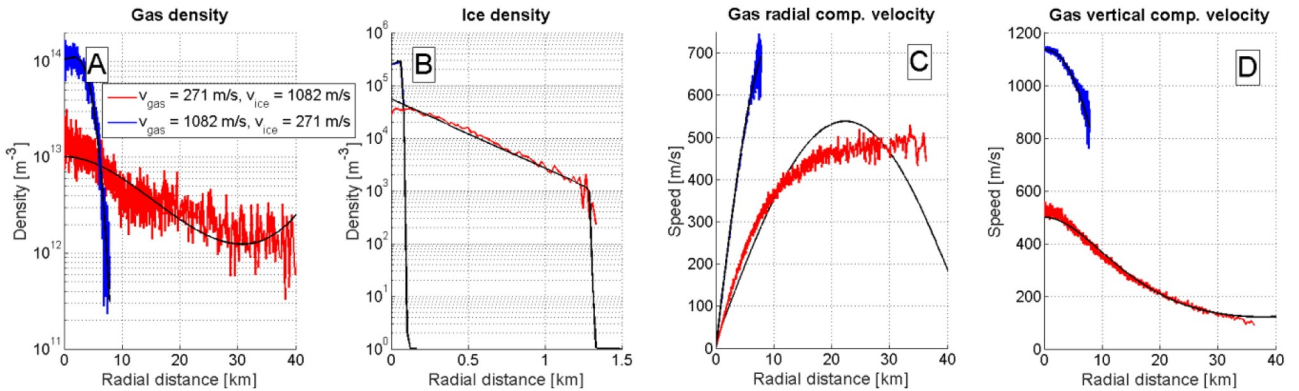

Fig. 5. Plume field interpolations at 10 km for two cases, in red (case A) the water vapor speed is equal to 271 m/s and the ice particle speed is equal to 1082 m/s, and in blue (case B) the water vapor speed is 1082 m/s while the ice particle speed is 271 m/s. Panel A is the water vapor number density in $[m^{-3}]$, Panel B is the ice particle number density in $[m^{-3}]$, Panel C is the water vapor radial speed in [m/s] and Panel D is the water vapor vertical speed in [m/s]. For each DSMC interpolation, the fit using the functional forms is given as the black curves. The RMS and the noise are given in Table 5. (For interpretation of the references to color in this figure legend, the reader is referred to the web version of this article.)

four times faster than the water vapor. However, Yeoh et al. (2017) does illustrate a "double throat" scenario in which grains accelerated by a first throat could be moving faster than vapor which interacts with conduit side walls further up. Case B, in contrast, could arise when ice particles are nucleated and grow in the boundary layer of the underground channel network or ricochet off the sidewalls, and thus have a lower speed than the water vapor. For the sake of completeness, we computed a broad range of velocity slip situations, which might or not have been observed in the CASSINI instruments measurements. As one can see, the situations close to the vent are very different. In Case A, the gas exits at very low speed compared to the ice particles. The gas molecules are accelerated by the interactions with the ice particles as they exit the vent. Since the water vapor molecules are exiting at low speed, they expand much more in the radial direction than in the default case, see Panel C. The gas expansion wave occurs close to the vent since the water vapor Mach number is small – $M = 1.5$, as seen in Panel A, and the ice particle column remains narrow, as shown in Panel B. On the contrary, in Case B, when the water vapor particles have a large speed

and the ice particles exit slowly, the ice particles are dragged laterally by the gas (see Panel F), which experience a much more extended expansion wave, as seen in Panel E. As shown in Panel F the ice particle column becomes much wider as it gains altitude than in Case A, since the collisions between ice particles and water vapor are much more frequent and the grains have time to expand before they convect too high, inducing a larger radial velocity component transfer between the water vapor and the ice grains. The ice particles radial profile is no longer radially homogeneous, while the velocity vectors remain more vertically oriented.

We note here that 1082 m/s slightly exceeds the theoretical ultimate speed possible for pure water vapor undergoing isentropic expansion from 273 K conditions, which would be 1009 m/s (Yeoh et al., 2015). This is reasonable, however, if we assume the flow not to be truly isentropic as it travels up the conduit, e.g. the nozzle flow was not ideal. Speeds higher than isentropic correspond to a case with slight heat conduction from the side walls of the vent.

We see that velocity slip between water vapor and ice particles, with

Table 5

Weighted root mean square (RMS) and weighted noise level for the interpolations of the simulations plotted in Fig. 5. The weights are the number of numerical particles in the cells, see Eqs. (3) and (4).

RMS interpolation / noise	Water vapor number density [log10(m^{-3})]	Ice grains number density [log10(m^{-3})]	Water vapor radial speed [m/s]	Water vapor vertical speed [log10(m/s)]
$v_{H_2O,ini}$ = 271 m/s $v_{ice,ini}$ = 1082 m/s	0.05/0.03	0.009/0.002	0.73/0.03	0.006/0.003
$v_{H_2O,ini}$ = 1082 m/s $v_{ice,ini}$ = 271 m/s	0.06/0.05	0.14/0.05	0.2/0.05	0.003/0.002

a lower speed for the ice particles, broadens the ice cone at high altitude, which could be a possible explanation of the observations by the ISS instrument on CASSINI that suggest an ice cone angle of up to 14° (Spitale et al., 2015). However, other characteristics of the outgassing flow could have the same effect, e.g. uniform-radius ice particles that are very small or a more realistic size-distribution of the ice grains with a sizable tail of small particles.

The samples at 10 km of these two cases are given in Fig. 5, where the color code is red for case A, i.e. the low water vapor speed and high ice grain speed, and blue for case B. The RMS between the functional form evaluation and the DSMC simulation interpolation at 10 km, together with the noise in the DSMC simulation are given in Table 5. All the RMS values are reasonable as compared to the noise. One can see that, for these two extreme cases, the radial profiles at 10 km have qualitatively different shapes. As mentioned earlier, while studying the effects of the initial speed variations of water vapor and the ice particles, we noticed that their variations were not linearly independent of the other variable. For this reason, we will consider the second-order cross-derivatives $\frac{\partial^2 \xi_k}{\partial v_{gas,ini} \cdot \partial v_{ice,ini}}$.

For the joint variations of the water vapor and ice particle speeds, we computed all $6 \times 6 - 1 = 35$ cases corresponding to the six speed values of either water vapor or ice particle speeds listed in Table 6.

4.3. Variation of the functional forms with the vent parameters

In order to compute the Jacobians $\frac{\partial \xi_k}{\partial \eta_j}$ and some of the Hessians $\frac{\partial^2 \xi_k}{\partial \eta_j \cdot \partial \eta_l}$, we define for each ξ_k a functional form $\xi_k = \xi_k(\eta_j)$ as a polynomial fit, see Section 3.2 above. The lists of polynomials, together with the values of their coefficients, are given in Tables 8 and 9. They are provided in Appendix A for continuity in the text. The degree of the polynomial can be inferred from the number of coefficients given in the tables, knowing that the polynomials are full, i.e. a polynomial expression in which all the coefficients are supposed to be non-zero, and in case of 2D interpolations, the polynomial degree is the same for both

Table 6

List of the varied vent parameters, together with their values, and the number of run cases. When the numbers follow a constant increment, we replaced the values by "…", i.e. the series 0.2, 0.4, 0.6, 0.8, 1 becomes 0.2, 0.4, …, 1. The default case values are set in bold.

Parameter	Symbol	Values	Number of runs
Factor to the mass flow	$f_{\dot{m}}$	0.1, 0.17, 0.32, 0.56, **1**, 1.8, 3.2, 5.6, 10	8
Gas speed [m/s]	$v_{gas,\ ini}$	271, 361, 542, 722, **902**, 1082	35
Ice speed [m/s]	$v_{ice,\ ini}$	271, 361, 542, 722, **902**, 1082	
Vent radius [m]	r_{vent}	0.2, 0.4, …, 1, 1.1, …, **1.4**, 1.5…, 2, 2.5, 3, 4, 5, 6	20
Grain radius [μm]	r_{ice}	0.01, 0.5, **1**, 2, 5	4
Ice mass ratio [%]	f_{ice}	0, 1, **5**, 10, 20, …, 80	10
Speed angle [°]	α_v	**0**, 1, …, 9	9
Temperature [K]	T_{ini}	33, 43, **53**, …, 143	11

variables. We center the abscissae of all polynomial fits by subtracting the default value of the vent parameter, i.e. we plot vs. $\xi_k - \xi_{k,0}$. Also, it should be noted that the fits for the factor to the mass flow $f_{\dot{m}}$, and for the radius of the ice particles r_{ice}, are performed on a decimal logarithmic scale, i.e. we fit $\log_{10}(\xi_k) - \log_{10}(\xi_{k,0})$. Finally, the 2D-polynomial-fitted values of the speed of water vapor and ice particles ($v_{gas, ini}$, $v_{ice,\ ini}$) are normalized by the speed of sound for a pure water vapor flow at the default vent condition, which is 180.4 m/s; thus, the abscissae turn out to be the water-vapor Mach number assuming the default vent conditions listed in Table 1.

4.4. Example: Variation of the ice mass loading

In Fig. 6 we present how variations of the ice mass loading conditions at the vent influence some of the water vapor and ice particle number densities and kinetic temperatures, together with the radial profile functional forms fits. Note that all the water vapor radial profiles are smoothed using a low-pass Fast Fourier Transform filter algorithm for clarity. The ice particle mass loading ratio obviously influences the magnitude of the number density profiles, see Panel A, since it directly affects the number density flow of each species at the vent. The ice particle mass loading also affects the width of the ice particle cone, see Panel B, which becomes narrower with larger ice particles mass loading. Hence, the number of ice particles is smaller, indicating that water vapor and ice particle collisions become less frequent, and the water vapor molecules are thus transferring less radial momentum to the ice particles. In panels C and D, we see that these variations modify the values for water vapor kinetic temperature in two ways: first the temperature in the region inside the ice particle cone varies with the ice particle mass loading. It has a maximum for ice particles mass loading of 10%. Second the temperature outside the ice particle region is directly correlated with the ice particle mass loading. Panel E shows that the ice particle kinetic temperature only drops slightly from the initial value of 53 K for these vent conditions, and the drop is slightly higher at low mass loading ratios. The kinetic temperature of the ice particles reflects their dispersion of velocities and in the limit of high drag where all ice particles move with the local gas velocity, one would expect the kinetic temperature to drop to near 0. At the nominal vent conditions there is poor coupling between ice grains and gas, so the velocity dispersion at 10 km altitude is not very different from the vent value, though it is slightly reduced at lower mass loading ratios (hence lower kinetic temperature) reflecting slightly better coupling between gas and grain motion. The length of the lines in Panel E reflects the effective radius of the ice cone at 10 km and shows that there is more spreading of the ice cone at low mass loadings reflecting the somewhat better coupling with the radially expanding gas. The ice particles follow nearly ballistic trajectories for high ice mass loading ratio. The dispersion in ice grain velocities at 10 km is important to predicting the subsequent trajectories of the ice particles as they move ballistically during further expansion of the plume above 10 km.

We provide the results of the DSMC simulations for all the cases listed in Table 1 – default cases – and Table 6 – variations to the default cases on the dropbox website https://utexas.box.com/v/MahieuxDSMCparam. The description of the repository can be found in Appendix C.
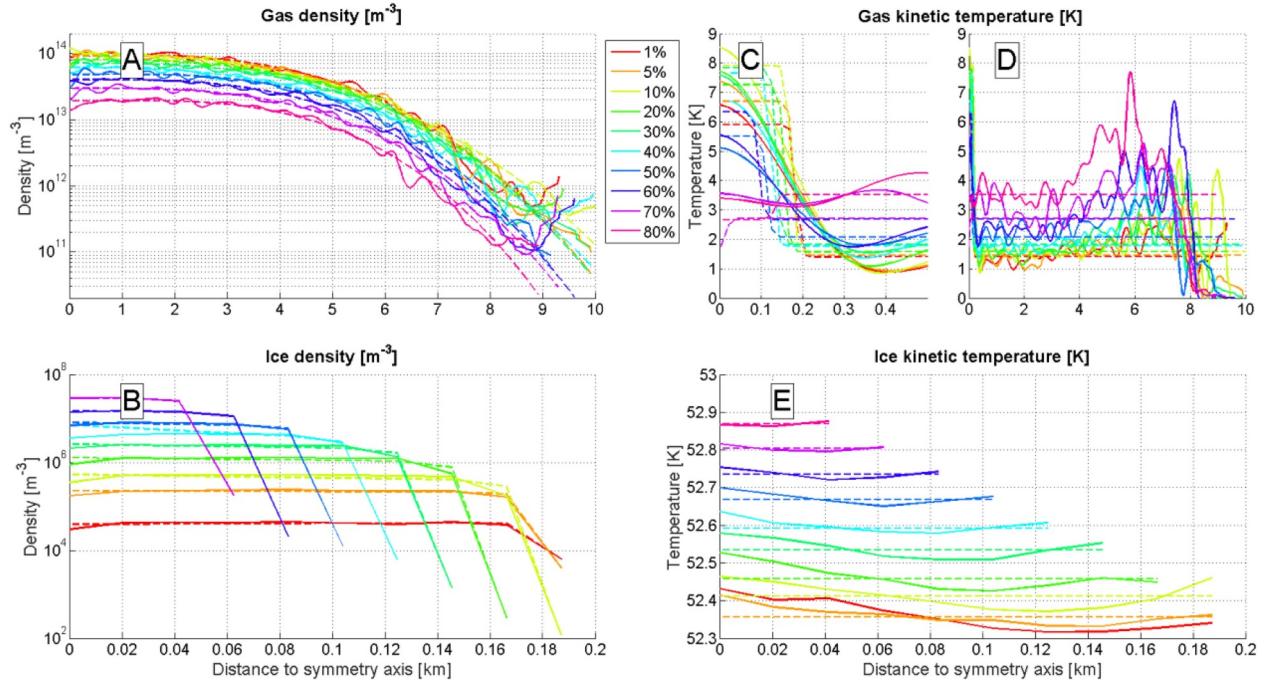
Fig. 6. Variation of some radial profiles as a function of the ice particle mass ratio conditions at the vent. Panel A: water vapor number density; Panel B: Ice particle number density; Panels C and D: water vapor kinetic temperature, close to the symmetry axis in Panel C, and for the whole radial domain in Panel D; and Panel E: Ice particle kinetic temperature. The color code is the ice mass loading f_{ice}, the legend is given in Panel A. The solid curves are the DSMC interpolations, the dashed curves are the functional form fits. For the water vapor number density (Panel A) and kinetic temperature (Panels C and D), a Fast Fourier Transform low-pass filter has been used for clarity. (For interpretation of the references to color in this figure legend, the reader is referred to the web version of this article.)

5. Discussion

In order to check the validity of the approach described in the previous sections, we ran several DSMC simulations while varying two or three vent parameters simultaneously, and checked the adequacy of the reproduction by the functional forms of the radial profiles of the number density, vertical and radial speeds and kinetic and rotational temperatures of both water vapor and ice particles. Table 7 summarizes the cases that have been run, together with the weighted RMS between the DSMC simulation results at 10 km and the reconstructed fits using

Table 7
List of the 23 DSMC runs varying two or three vent parameters. The first column is the Case number, the columns 2–9 are the vent parameter values; the ones that are different from the default values are shaded. The columns 10–18 give the RMS of the reconstructed fits using the interpolations of the functional forms coefficients. The shaded cells in the right part of the table are the ones for which the profiles are presented in Fig. 7. The RMS values that are given for v_{ice} in the table are multiplied by 1000.

| Case #	$f_{\dot{m}}$	r_{vent}	$v_{gas, ini}$	$v_{ice, ini}$	r_{ice}	f_{ice}	α_v	T_{ini}	n_{gas}	v_{gas}	u_{gas}	$T_{rot, gas}$	$T_{kin, gas}$	n_{ice}	v_{ice}	u_{ice}	$T_{kin, ice}$
Default	1	1.4	902	902	1	0.05	0	53	0.065	0.0036	0.1889	0.0585	0.3161	0.0236	0.0341	0.0254	0.0013
1	0.5	1.6	902	902	1	0.05	0	53	0.069	0.0049	0.2568	0.0647	0.4080	0.0647	0.0346	0.0532	0.0056
2	2.5	1.4	577	902	1	0.05	0	53	0.047	0.0093	0.3250	0.0472	0.2489	0.0472	15.1538	0.1536	0.2678
3	1.8	1.4	902	740	1	0.05	0	53	0.059	0.0031	0.1900	0.0587	0.3318	0.0587	7.5049	0.0518	0.0802
4	3.7	1.4	902	902	1	0.11	0	53	0.063	0.0030	0.1656	0.0576	0.2373	0.0576	0.1667	0.0167	0.0181
5	0.49	1.4	902	902	1	0.05	2.1	53	0.074	0.0047	0.2444	0.0620	0.4301	0.0620	0.0737	0.0789	0.0052
6	0.4	1.4	902	902	1	0.05	0	150	0.084	0.0091	0.6318	0.0637	1.0206	0.0637	0.8590	0.0400	0.0268
7	1	3	577	902	1	0.05	0	53	0.065	0.0074	0.3187	0.0753	0.2290	0.0753	12.2660	0.1277	0.2392
8	1	0.9	902	198	1	0.05	0	53	0.082	0.0048	0.3385	0.0793	1.2660	0.0793	33.3462	0.2823	1.1230
9	1	1.5	902	902	1	0.02	0	53	0.070	0.0042	0.2231	0.0639	0.3296	0.0639	0.0679	0.0185	0.0030
10	1	1.8	902	902	1	0.05	5	53	0.075	0.0033	0.1956	0.0597	0.3428	0.0597	0.1131	0.0626	0.0093
11	1	2.1	902	902	1	0.05	0	80	0.073	0.0052	0.2916	0.0557	0.3836	0.0557	0.2594	0.0254	0.0119
12	1	1.4	361	992	1	0.05	0	53	0.061	0.0056	0.6418	0.0551	0.3355	0.0551	1.2898	0.0210	0.3799
13	1	1.4	541	631	1	0.05	0	53	0.060	0.0054	0.3448	0.0559	0.3210	0.0559	0.1376	0.0197	0.0133
14	1	1.4	469	379	1	0.05	0	53	0.064	0.0045	0.4232	0.0542	0.5627	0.0542	0.6476	0.0128	0.0084
15	1	1.4	325	902	1	0.12	0	53	0.063	0.0091	0.6952	0.0514	0.2525	0.0514	1.4415	0.2301	0.0884
16	1	1.4	613	902	1	0.05	6	53	0.071	0.0085	0.3615	0.0589	0.3152	0.0589	1.5779	0.0226	0.0819
17	1	1.4	433	902	1	0.05	0	30	0.071	0.0121	0.4730	0.0905	0.3461	0.0905	6.0584	0.0422	0.4768
18	1	1.4	902	559	1	0.22	0	150	0.070	0.0118	0.5638	0.0638	0.8759	0.0638	5.0407	0.0615	0.1228
19	1	1.4	902	776	1	0.05	3	53	0.073	0.0038	0.2294	0.0557	0.4278	0.0557	0.7260	0.0588	0.0232
20	1	1.4	902	289	1	0.05	0	100	0.078	0.0055	0.3584	0.0615	0.7613	0.0615	4.5220	0.1297	0.7311
21	1	1.4	902	902	1	0.08	1.5	53	0.070	0.0038	0.2013	0.0597	0.3299	0.0597	0.0468	0.0274	0.0022
22	1	1.4	902	902	1	0.12	0	110	0.068	0.0062	0.3607	0.0638	0.4894	0.0638	0.0481	0.0173	0.0033
23	1	1.4	902	902	1	0.05	4	88	0.072	0.0049	0.3102	0.0675	0.5224	0.0675	0.1242	0.0286	0.0065
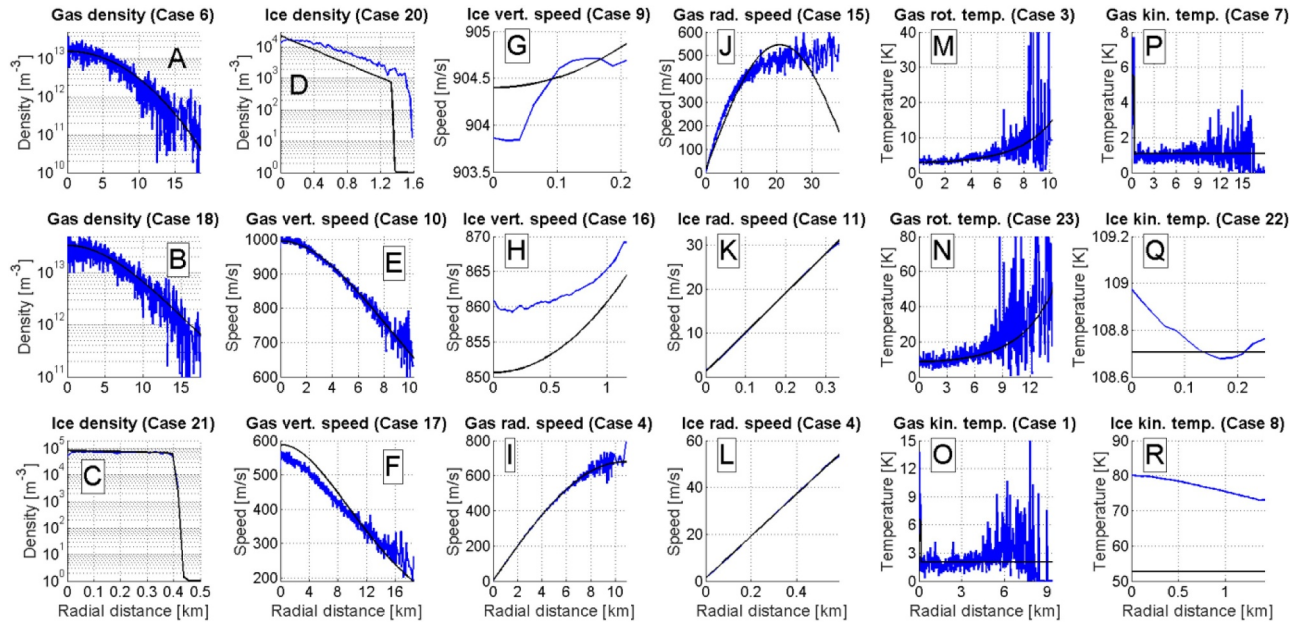
Fig. 7. Comparison between interpolations at 10 km of DSMC simulations and polynomial evaluation of the functional form coefficients for cases varying two to three vent parameters from the default value. In each subplot, the DSMC extractions at 10 km of the radial profiles are the blue curves, while the evaluation of the functional forms using the fitted polynomial coefficients are given by the black curves. In the title of each subplot, the physical quantity and the case number, as listed in Table 7, are given. Panels A and B show results for the water vapor number density profiles, Panels C and D are ice particle number density profiles, Panels E and F are water vapor vertical component of the velocity profiles, Panels G and H are ice particle vertical component of the velocity profiles, Panels I and J are water vapor radial component of the velocity profiles, Panels K and L are ice particles radial component of the velocity profiles, Panels M and N are water vapor rotational temperature profiles, Panels O and P are water vapor kinetic temperature profiles and Panels Q and R are ice particle kinetic temperature profiles. (For interpretation of the references to color in this figure legend, the reader is referred to the web version of this article.)

the expressions described in the previous sections. Fig. 7 shows the profiles for some cases, for which the corresponding cells are shadowed in Table 7. For each physical quantity of each species, we tried to show both a "good" and "bad" example of reconstructed fits to give the reader an idea of the quality of the results.

For the sake of the method clarity, we present the expressions used to reconstruct the profiles of case 1 from Table 7 in Appendix B, where we varied both the mass flow $f_{\dot{m}}$ and the radius of the vent r_{vent} simultaneously to the values $\hat{f}_{\dot{m}} = 0.5$ and $\hat{r}_{vent} = 1.6$ m – the default values are 1 and 1.4 m.

The expressions describing the other physical radial profiles are built similarly. Note that no formal differentiation of the polynomial expressions is needed since the polynomials are centered on the default vent parameter values.

The right part of Table 7 considers how well DSMC results are predicted by our parametrizations. We consider general vent parameter values and evaluate the radial profiles using the interpolation of the parameterized functional forms. We run DSMC calculations for these vent parameters and fit the values at 10 km. We evaluate the RMS between these two profiles and report it in Table 7. Considering water vapor, all the RMS values of the Cases of Table 7 for the number density, vertical and radial components of the speed and kinetic and rotational temperature are of the same order of magnitude as the default case, that is reported in Table 5. For the ice particles, the RMS values of the Cases of Table 7 are of the same order of magnitude for the number density and radial component of the velocity, while some discrepancies are seen for the kinetic temperature and the vertical component of the speed. We attribute this to the fact that the fits are harder to obtain for the water ice particles, since the ice cone is much narrower, and thus has non-zero values in fewer cells, and that the numerical noise in the DSMC simulations is also larger due to fewer simulated ice particles.

However, in most of the cases, the vertical component of the speed and the kinetic temperature can be correctly reproduced.

We have shown that we can easily and quickly reconstruct the radial profiles at 10 km, in a very quick and sufficiently reliable way with these expressions. In these examples, we did not consider extrapolations of the radial profiles functional forms, i.e. the chosen values of the vent parameters are within the intervals of the varied values listed in Table 6. We observed that the reliability of the reconstructed radial profiles degrade quickly when the values are taken outside of the intervals, because of the non-linearity of the processes that we are simulating here.

6. Conclusion and future work

In this work, we built more than 100 accurate spatially and temporally resolved, but computationally expensive, DSMC simulations of single Enceladus water geysers, from which we extracted the physical parameters at an altitude of 10 km, where the flow is non-collisional. Each DSMC simulation took more than 48 h using four processors to complete.

We extracted the water vapor and ice particle number density, vertical and radial velocity and kinetic temperature, and the water vapor rotational temperature. We varied the most relevant physical parameters at the vent: the mass flow, the vent radius, the ice particle radius, the ice particle to total flow mass ratio, the water vapor exit speed, the ice particle exit speed, the water vapor and ice particle exit temperature and the vent exit angle. We modeled the radial profiles at 10 km altitude using simple functional forms. Finally, we studied the variations of the functional form coefficients as a function of the vent parameters, assuming that they are linearly independent. For the water vapor and ice particle vent exit speeds, we found out that this condition of linear independence is not fulfilled while varying the two variables

Table 8

List of the polynomial coefficients to be used to reconstruct the radial profiles at 10 km using the functional forms defined in Table 3. The coefficient names (first column) correspond to the ones from that table. The polynomials are computed using an abscissae equal to the difference of the desired vent parameter η_j and the corresponding default vent value $\eta_{j,\,0}$, i.e. $\eta_j - \eta_{j,0}$, which are given in Table 1. For the variations relative to the factor to the mass flow $f_{\dot{m}}$ and the grain radius r_{ice}, the decimal logarithm is considered. They are marked with a * in the table. The coefficients are sorted in ascending order, i.e. $\xi_k = c_0 + c_1 \cdot (\eta_j - \eta_{j,0}) + c_2 \cdot (\eta_j - \eta_{j,0})^2 + \dots$

Coeff. name	Coefficients of the polynomials in ascending order					
	$f_{\dot{m}}^*$	r_{vent}	r_{ice}^*	f_{ice}	α_v	T_{ini}
a_0	13.968; 0.98118	13.968; 0.80116; -0.24988; 0.030186	13.968	13.968; -0.0029181; $-4.2155-05$; $-5.1858-07$	13.968; 0.010725	13.968; -0.0077314; 0.00010618; $-6.9274e-07$
a_2	0.089322; -0.65648	0.089322; -0.16792; -0.20098; 0.042995	0.089322	0.089322; 0.0036286	0.089322; -0.49925; 0.0061709	0.089322; 0.0072651; -0.0020932; 1.8123e-05
a_3	-3.3823; 1.0152	-3.3823; -0.37852; 0.35652; -0.061889	-3.3823	-3.3823; 0.001354	-3.3823; 0.60672; -0.011522	-3.3823; 0.029853; 0.0015136; $-1.4766e-05$
b_0	2.6778; -0.42165; 0.0056003; -0.11877; 0.023835; 0.12368	2.6778; 0.0093396; -0.0026547; 0.00055535	2.6778; -0.61727; 0.11535	2.6778; 0.047619; -0.0011723; 1.0817-05	2.6778; -0.29598; 0.049413; -0.0046131; 0.00016447	2.6778; -0.0039627; 2.3364-05; $-1.7823e-07$; 1.4177e-09
b_1	-0.095984	-0.095984; 0.17489; -0.061139; 0.0066353	-0.095984	-0.095984; -0.0096515	-0.095984; 0.0092808	-0.095984
b_2	0.19084; 0.41336; 0.44225; 0.24574; 0.01536; -0.019727	0.19084; 0.12386; -0.0041885	0.19084; -0.4521; 0.48663; -0.070205	0.19084; -0.0018883	0.19084; 0.15465; 0.0012067; 4.0581-05	0.19084; 0.0017856; $-7.7984e-06$; 1.063e-08; 2.4086e-10
c_0	2.9986; 0.0018836; -0.00069996	2.9986; 0.0021094; -0.0013; 0.00018594	2.9986	2.9986; $-8.7765-05$	2.9986; -0.00019368	2.9986; 0.00072202; $-1.316e-06$; 9.2593e-10
c_1	0.036289; 0.0040976; 0.0059829; -0.0076116	0.036289; 0.0017074; -0.00060254; 5.6196-05	0.036289	0.036289; 5.4508-05; $-1.8486-06$	0.036289; 0.00054907	0.036289; 1.0746e-05; 1.9451e-07
c_2	$-1.4461-06$; -0.0010638; -0.00060035; 0.0010703	$-1.4461-06$; -0.00041255; 0.00014437; $-1.4537-05$	$-1.4461-06$	$-1.4461-06$; $-1.6051-05$; 4.4934-07	$-1.4461-06$; $-7.9817-05$	$-1.4461e-06$; $-1.003e-05$; 3.4684e-08
d_0	2.9562; 0.0035572; 0.0041919; 0.0028983	2.9562; 0.0011112; $-1.8745-05$	2.9562; -0.0036047; 0.0035311; -0.0011631	2.9562; $-1.4217-05$; $-3.4902-08$	2.9562; 0.00017296; $-1.4112-05$	2.9562; 3.1999e-05
d_2	0.00018794; 0.00054879; -0.00079573; -0.0031883	0.00018794; 3.103-06; 2.017-06; $-7.4237-06$	0.00018794; 0.01198	0.00018794; $-5.1843-06$; 3.8242-08	0.00018794; -0.00029598; -0.00021295; 8.2645-06; $-6.3586-07$	0.00018794; 1.3091e-06
e_0	638.58; 71.995; -15.716	638.58; 30.118; -8.3784; 0.67; 0.018836	638.58	638.58; 0.43915; -0.0047732; -0.00018484	638.58; 4.1031	638.58; 2.7201
e_1	0.15562; -0.018193; 0.0047651	0.15562; -0.0077896; 0.0020217; $-5.5177-05$; $-2.1373-05$	0.15562	0.15562; -0.00010623; $-6.1874-07$; 7.6476-08	0.15562; -0.0013629	0.15562; -0.0004192
e_2	1.6011	1.6011	1.6011	1.6011; -0.014776	1.6011	1.6011; -0.013997; 0.00075375
f_0	1.2261; -0.27398; 0.33861	1.2261; -0.061441; 0.028607; -0.0036041	1.2261; -0.31433	1.2261; 0.0031329; 9.7754-05; $-1.9698-06$	1.2261; -0.039922; 0.00686; $-3.8038-05$	1.2261; -0.00026425; $-1.318e-06$
f_1		86.67; 3.8803;	86.67; -3.5075		86.67; 1.7902;	86.67; 0.029315

(continued on next page)

Table 8 (*continued*)

Coeff. name	Coefficients of the polynomials in ascending order					
	$f_{\dot{m}}*$	r_{vent}	$r_{ice}*$	f_{ice}	α_v	T_{ini}
	86.67; 9.8838; −4.8173	−1.5973; 0.20261		86.67; −0.085003; −0.0019971	−0.32668; 0.01642	
g_0	0.61752; −0.6365	0.61752; −0.18348; 0.13237; −0.049376; 0.0056523	0.61752	0.61752; 0.0037953; 3.0418−05	0.61752; 0.0032737	0.61752; 0.010217; −4.1064e−05
g_2	0.006979	0.006979; 0.0002908; 2.4876−05	0.006979; 0.00039019	0.006979; −7.2981−06	0.006979; −0.00013163	0.006979; −9.7987e−05; 4.9385e−07
h_0	1.462; −1.8593; 1.1633; −0.30396	1.462; −0.4034; 0.32437; −0.12836; 0.016283	1.462	1.462; 0.0016934; 0.00031733	1.462	1.462; 0.031121
h_1	2.6169; 0.22768; −2.7188	2.6169; −0.26334; −0.016747	2.6169; 1.4869	2.6169; −0.02341	2.6169; −0.29357	2.6169; 0.086623; 0.001027
h_2	0.17917; 0.44848; 0.561	0.17917; 0.12434; −0.0060578; 0.00029692	0.17917; −0.21214; −0.12415	0.17917; −0.0019432; 9.894−06	0.17917; 0.12384	0.17917; 0.0017668; −4.8333e−06
i_0	52.356; −1.5322; −2.1881; −1.3201	52.356; −0.45065; 0.0088982; −0.00179	52.356; 3.3654; −4.4667	52.356; 0.0068715	52.356; 0.043175; −0.12597; 0.069675; −0.017952; 0.0024091; −0.00016272; 4.3778−06	52.356; 0.98772
j_0	9.9161; 0.58793	9.9161; 0.96353; −0.21206; 0.017199	9.9161; −0.31295	9.9161; −0.0067658	9.9161; 0.21115; 0.00027489	9.9161; 0.035045; 0.001649; −1.2443e−05
k_0	0.18714; 0.43332; 0.462; 0.20289	0.18714; 0.12722; −0.0072152; 0.00050442	0.18714; −0.47713; 0.44463; −0.084651	0.18714; −0.00017278; −0.00011419; 3.0004e−06; −3.5916e−08; 1.6027e−10	0.18714; 0.16002; −0.00063746; 0.00020047; −3.0532e−06	0.18714; 0.001998; −1.1041e−05; 1.109e−08; 3.6968e−10

simultaneously, implying that we needed to consider the cross-correlation between these two variables. With that caveat, however, we have developed parametrizations of the flow parameters – water vapor and ice particle number density, vertical and radial components of the velocity and kinetic temperature, and water vapor rotational temperature – at 10 km, that can be evaluated in a few milliseconds.

After deriving all the coefficients mentioned above, we verified the validity of the approach for 23 test cases, by varying two or three vent parameters simultaneously, and, separately, computing the geyser fields using our DSMC code. We compared the DSMC extractions at 10 km with the results of our parametrization.

To evaluate the quality of the fits, we consider the weighted RMS of the DSMC simulations with respect to the results of the parametric interpolation, and we show that in most of the cases the RMS is within an acceptable range of a reference RMS.

One of the principal limitations of the current approach is that we consider a uniform radius for the ice particles. Another limitation is that we assumed equal kinetic temperature for the water vapor and water ice grains at the vent though some studies show that the water ice grains might have slightly larger kinetic temperature. In future work, we will model a particle size distribution and its effect on the flow at

10 km and consider different kinetic temperatures for the two water phases.

These parametrizations of the Enceladus water geysers can be used to supply the relevant information to free molecular/ballistic codes, in order to propagate the geyser into space, since the geysers are free molecular above these altitudes. The results from the DSMC analysis can be provided upon request by emailing any author of the paper.

We provide on an online dropbox website the results of the DSMC simulations that have been used to calculate the parametrizations presented in this work: https://utexas.box.com/v/MahieuxDSMCparam.

Note that the parametrizations were calculated for an altitude of 10 km, but results can also be obtained at lower altitudes.

Table 9

List of the 2D polynomial coefficients to be used to reconstruct the radial profiles at 10 km using the functional forms defined in Table 3 for the water vapor and ice particle speeds. The coefficients name (first column) correspond to the ones from Table 3, the second column gives the order of the polynomial, which is equal for both variables. The polynomials are computed using an abscissae equal to the difference of the desired vent parameter η_j and the corresponding default vent value $\eta_{j,0}$, i.e. $\eta_j - \eta_{j,0}$, which are given in Table 1. The coefficients η_j and $\eta_{j,0}$ for the speeds are normalized by the value 180.4, which is equivalent to the speed of sound for water vapor at the vent for the default vent conditions. The coefficients are sorted in ascending order, i.e. $\xi_k = c_{00} + c_{10} \cdot (v_{gas} - v_{gas,ini}) + c_{01} \cdot (v_{ice} - v_{ice,ini}) + c_{20} \cdot (v_{gas} - v_{gas,ini})^2 + c_{11} \cdot (v_{gas} - v_{gas,ini}) \cdot (v_{ice} - v_{ice,ini}) + c_{02} \cdot (v_{ice} - v_{ice,ini})^2 + ...$

Coeff. name	Coefficients of the 2D polynomials ($v_{gas,\,ini}$, $v_{ice,\,ini}$) in ascending order
a_0	13.968; 0.13891; −0.0053748; 0.0020492; 0.012051; 0.0012839; 0.011825; 0.0040657; −0.00066404; 0.0014769
a_2	0.089322; 1.2471; 0.05196; −0.6999; −0.10609; −0.11303; −0.010071; −0.18344; −0.20528; 0.076165; 0.11064; −0.056665; −0.1084; −0.041586; 0.069188; 0.016625; −0.0021695; −0.011045; −0.017556; 0.0028801; 0.010217
a_3	−3.3823; −1.4451; −0.24333; 0.66392; 0.20541; 0.31321; 0.01008; 0.11966; 0.14744; 0.16537; −0.036041; 0.020833; 0.022388; 0.019574; 0.019292
b_0	2.6778; 0.001617; 0.12401; −0.020847; 0.027357; −0.014919; −0.014799; −0.015371; 0.017023; −0.016805; −0.0047741; −0.0069959; 0.0034067; −0.00077036; −0.0051172; −0.00062284; −0.00072585; −0.00082238; 0.0016875; −0.00063412; −0.00058279
b_1	−0.095984; −0.40557; 0.089013; 0.011761; 0.074186; −0.10328; 0.1784; 0.046252; 0.042654; 0.029182; 0.069433; 0.030322; 0.034097; −0.013733; 0.033848; 0.0077527; 0.0062882; −0.0008533; 0.0073856; −0.0041461; 0.0051507
b_2	0.19084; 0.018613; −0.067138; 0.0082378; −0.039831; 0.03088; 0.012194; −0.0099834; 0.012284; −0.008256; 0.0058428; 0.00085879; −0.0015416; 0.0013605; 0.0016231; 0.00090738; 0.00033069; −0.00073994; 0.0023344; −0.0015711; 7.2217e−05
c_0	2.9986; 0.068639; 0.0014668; −0.0041199; −0.00015779; −0.00060025; 0.00032026; 0.00022516; −9.7046e−05; −0.00013299
c_1	0.036289; −0.0036923; −0.00054457; −3.4017e−05; −6.9753e−05; −0.00053441; 0.00031933; 0.00014248; −0.00016872; −4.494e−05
c_2	−1.4461e−06; 0.00076198; 0.00024303; 0.0002357; 8.9974e−05; 8.1473−05; 1.4203−05; −3.2045−07; 2.8668−05; −4.4621−07
d_0	2.9562; 0.019238; 0.066563; 0.0024613; −0.0099342; −0.0015783; 0.0014812; −0.003599; 0.0056403; −0.0020818; 0.00068577; −0.00064804; 0.00031915; 9.8482−05; −0.00010001; 9.1723−05; −5.81−05; −0.00037582; 0.00077491; −0.0002431; −1.7781−05
d_2	0.00018794; −0.011358; 0.011125; −0.0011058; 0.0040022; −0.0030111; 0.00050681; 0.00052661; −0.0016782; 0.00078995; 0.00031547; 0.00019821; −0.00018964; 1.2367−05; −0.00021848; 5.8257−05; 7.0162−05; 2.8142−05; −0.00029875; 0.00021423; −5.0233−05
e_0	638.58; 53.308; 0.46277; 10.021; −5.6504; 2.8999; 4.4842; 1.5162; 0.33677; −1.9531; 1.0153; 1.0884; −0.28443; 0.3169; −0.60915
e_1	0.15562; 0.011672; 0.0017068; −0.0032822; 0.0031789; −0.0020574; 0.00075758; 0.00050507; 0.00076567; −0.0010454; 0.00015417; −0.00021877; 0.00038588; −3.7398−05; −0.0001605
e_2	1.6011; 0.041622; 0.16075; −0.04306; 0.22508; −0.06814; −0.27344; −0.23671; −0.13695; −0.056725; 0.030351; −0.069605; −0.038625; −0.044204; −0.0087532
f_0	1.2261; 0.096406; 0.15879; 0.024411; −0.048425; 0.015746; 0.0063887; −0.0044908; −0.0028672; −0.0053377; 0.0012617; 0.0025727; −0.0022451; −0.0076245; 0.005065
f_1	86.67; 3.4; 12.909; 0.91815; −1.4211; 0.32553; 0.073836; −0.08155; 0.15777; −0.17561; −0.027174; 0.10271; −0.09558; 0.027779; −0.011755
g_0	0.61752; 0.014261; −0.0093821; 0.0046367; −0.0079539; 0.0051359
g_2	0.006979; 0.0033259; 0.00022917; 0.00039842; 6.945−05; −3.2679−06
h_0	1.462; 0.12052; −0.025741; 0.033441; −0.043414; 0.015409; 0.0065483; −0.0075721; −0.0025168; 0.0032292
h_1	2.6169; 0.88582; −2.5165; 0.51457; −2.441; 2.0372
h_2	0.17917; 0.014424; −0.067898; −0.0080072; −0.025864; 0.060667
i_0	52.356; −0.71191; 0.052765; −1.5662; 0.82194; 0.46798; −0.37588; 0.45732; −0.15432; 0.78288; −0.21268; 0.26296; −0.11722; 0.31378; −0.0583; −0.0043065; 0.028235; 0.020553; −0.026928; 0.038485; −0.0062704; −0.0076752; 0.016595; −0.015485; 0.01239; −0.0055992
j_0	9.9161; −2.3687; 0.023669; 1.162; −0.54025; −0.55919; −0.1491; 0.56192; 0.24097; −0.52931; −0.18108; 0.15693; 0.4517; 0.23182; −0.17486; −0.05295; −0.028158; 0.043256; 0.095409; 0.032905; −0.020111
k_0	0.18714; 0.0049202; −0.066148; −0.0046025; −0.034851; 0.03923; 0.022538; −0.008497; 0.0096337; −0.012484; 0.01411; −0.0026211; −0.00043154; 0.00080616; −0.0033325; 0.0022094; −0.00067773; 7.527−07; 0.0018591; −0.0015015; −0.00078583

Supplementary materials

Supplementary material associated with this article can be found, in the online version, at doi:10.1016/j.icarus.2018.10.022.

Appendix A. List of the polynomial coefficients to evaluate the functional forms

.

Appendix B. Evaluation of the functional forms based on the polynomial regressions

Expansion of the expression used to reconstruct the profiles of case 1 from Table 7, where we varied both the mass flow $f_{\dot{m}}$ and the radius of the vent r_{vent} simultaneously to the values $\hat{f}_{\dot{m}} = 0.5$ and $\hat{r}_{vent} = 1.6$ m – the default values are 1 and 1.4 m.

$$\log_{10}(n_{H_2O}(x; f_{\dot{m}}, r_{vent})) = a_0(f_{\dot{m}}, r_{vent}) + a_2(f_{\dot{m}}, r_{vent}) \cdot \left(\frac{x}{W_{H_2O}(f_{\dot{m}}, r_{vent})}\right)^2 + a_3(f_{\dot{m}}, r_{vent}) \cdot \left(\frac{x}{W_{H_2O}(f_{\dot{m}}, r_{vent})}\right)^3$$

$$= \left\{\begin{bmatrix} \overset{13.968}{\widetilde{a_{0,f_{\dot{m}},0}}} + \overset{0.98118}{\widetilde{a_{0,f_{\dot{m}},1}}} \cdot \left(\log_{10}(\hat{f_{\dot{m}}}) - \log_{10}\left(\widetilde{\frac{1}{f_{\dot{m},0}}}\right)\right) \end{bmatrix} \\ + \begin{bmatrix} \overset{0.80116}{\widetilde{a_{0,r_{vent},1}}} \cdot \left(\hat{r}_{vent} - \overset{1.4}{\widetilde{r_{vent,0}}}\right) + \overset{-0.24988}{\widetilde{a_{0,r_{vent},2}}} \cdot \left(\hat{r}_{vent} - \overset{1.4}{\widetilde{r_{vent,0}}}\right)^2 + \overset{0.030186}{\widetilde{a_{0,r_{vent},3}}} \cdot \left(\hat{r}_{vent} - \overset{1.4}{\widetilde{r_{vent,0}}}\right)^3 \end{bmatrix} \right\}$$

$$+ \left\{\begin{bmatrix} \overset{0.089322}{\widetilde{a_{2,f_{\dot{m}},0}}} + \overset{-0.65648}{\widetilde{a_{2,f_{\dot{m}},1}}} \cdot \left(\log_{10}(\hat{f_{\dot{m}}}) - \log_{10}\left(\widetilde{\frac{1}{f_{\dot{m},0}}}\right)\right) \end{bmatrix} \\ + \begin{bmatrix} \overset{-0.16792}{\widetilde{a_{2,r_{vent},1}}} \cdot \left(\hat{r}_{vent} - \overset{1.4}{\widetilde{r_{vent,0}}}\right) + \overset{-0.20098}{\widetilde{a_{2,r_{vent},2}}} \cdot \left(\hat{r}_{vent} - \overset{1.4}{\widetilde{r_{vent,0}}}\right)^2 + \overset{0.042995}{\widetilde{a_{2,r_{vent},3}}} \cdot \left(\hat{r}_{vent} - \overset{1.4}{\widetilde{r_{vent,0}}}\right)^3 \end{bmatrix} \right\} \cdot \left(\frac{x}{W_{H_2O}(f_{\dot{m}}, r_{vent})}\right)^2$$

$$+ \left\{\begin{bmatrix} \overset{-3.3823}{\widetilde{a_{3,f_{\dot{m}},0}}} + \overset{1.0152}{\widetilde{a_{3,f_{\dot{m}},1}}} \cdot \left(\log_{10}(\hat{f_{\dot{m}}}) - \log_{10}\left(\widetilde{\frac{1}{f_{\dot{m},0}}}\right)\right) \end{bmatrix} \\ + \begin{bmatrix} \overset{-0.37852}{\widetilde{a_{3,r_{vent},1}}} \cdot \left(\hat{r}_{vent} - \overset{1.4}{\widetilde{r_{vent,0}}}\right) + \overset{0.35652}{\widetilde{a_{3,r_{vent},2}}} \cdot \left(\hat{r}_{vent} - \overset{1.4}{\widetilde{r_{vent,0}}}\right)^2 + \overset{-0.061889}{\widetilde{a_{3,r_{vent},3}}} \cdot \left(\hat{r}_{vent} - \overset{1.4}{\widetilde{r_{vent,0}}}\right)^3 \end{bmatrix} \right\} \cdot \left(\frac{x}{W_{H_2O}(f_{\dot{m}}, r_{vent})}\right)^3$$

where

$$W_{H_2O}(f_{\dot{m}}, r_{vent}) = \begin{bmatrix} \overset{9.9161}{\widetilde{j_{0,f_{\dot{m}},0}}} + \overset{0.58793}{\widetilde{j_{0,f_{\dot{m}},1}}} \cdot \left(\log_{10}(\hat{f_{\dot{m}}}) - \log_{10}\left(\widetilde{\frac{1}{f_{\dot{m},0}}}\right)\right) \end{bmatrix} + \begin{bmatrix} \overset{0.96353}{\widetilde{j_{0,r_{vent},1}}} \cdot \left(\hat{r}_{vent} - \overset{1.4}{\widetilde{r_{vent,0}}}\right) + \overset{-0.21206}{\widetilde{j_{0,r_{vent},2}}} \cdot \left(\hat{r}_{vent} - \overset{1.4}{\widetilde{r_{vent,0}}}\right)^2 + \overset{0.017199}{\widetilde{j_{0,r_{vent},3}}} \cdot \left(\hat{r}_{vent} - \overset{1.4}{\widetilde{r_{vent,0}}}\right)^3 \end{bmatrix}$$

In this expression, we wrote above the coefficients their numerical values, taken from Table 1 and Table 8.

Appendix C. Description of the FTP repository containing the DSMC simulations

The results of the DSMC simulations are available on the dropbox repository https://utexas.box.com/v/MahieuxDSMCparam. The data are given as MATLAB binary file.

The structure of the repository is as follow. There is one directory for each simulation. The name of the directory corresponds to the vent parameter that is varied, see Table 6, followed by the considered value(s) X (and Y), separated by un underscore, with the following keywords:

- Factor to the mass flow ($f_{\dot{m}}$): *Den_X* with X having the format (0)0.00
- Vent radius (r_{vent}): *Radius_X* with X having the format 0.0
- Grain radius (r_{ice}): *GrainSize_X* with X having the format 0.00
- Ice mass ratio (f_{ice}): *MRatio_X* with X having the format 00
- Speed Angle (α_v): *Angle_X* with X having the format 00
- Temperature (T_0): *Temp_X* with X having the format (0)00
- Gas speed and Ice speed ($v_{gas,\,0}$ and $v_{ice,\,0}$): *Gv_X_Iv_Y* with X and Y having the format 0(0.0)

The Default case is given under the directory *Default*.

In each directory, eight MATLAB files are given corresponding to the eight stages of the DSMC calculation, with their names being the name of the directory, followed by un underscore, the letters *stg*, the stage number and the letters *_all.mat*. For example, the file corresponding to the third stage for a speed angle of 3° is *Angle_03_stg3_all.mat*.

Each MATLAB binary file contains one single variable named *resmat*. The number of lines corresponds to the number of cells considered in the stage, while the 22 columns are the values of the different variables for that stage, with the position given in left-handed spherical coordinates and the speed vector components given in Cartesian coordinates:

1 Polar angle ϕ [rad]
2 Radial distance r [km]
3 Azimuthal angle θ [rad]
4 Number of molecules (mixture of water vapor and water ice particles) n [m^{-3}]
5 X speed vector component (mixture of water vapor and water ice particles) U [m/s]
6 Y speed vector component (mixture of water vapor and water ice particles) V [m/s]
7 Z speed vector component (mixture of water vapor and water ice particles) W [m/s]
8 Kinetic temperature (mixture of water vapor and water ice particles) T_{kin} [K]
9 Number of numerical molecules (mixture of water vapor and water ice particles) n_{num} [1]
10 Cell volume V_{cell} [m^3]
11 Numerical weight ratio for the water vapor f_{num} [1]
12 Water vapor local number density n_{gas} [m^{-3}]
13 Water vapor rotational temperature $T_{rot,\,gas}$ [K]
14 Water vapor kinetic temperature $T_{kin,\,gas}$ [K]

15 Water vapor X speed vector component U_{gas} [m/s]
16 Water vapor Y speed vector component V_{gas} [m/s]
17 Water vapor Z speed vector component W_{gas} [m/s]
18 Water ice particle local number density n_{ice} [m^{-3}]
19 Water ice particle kinetic temperature $T_{kin,\ ice}$ [K]
20 Water ice particle X speed vector component U_{ice} [m/s]
21 Water ice particle Y speed vector component V_{ice} [m/s]
22 Water ice particle Z speed vector component W_{ice} [m/s]

For each stage, the values are only given for the stage itself, and not at the position of the inner stages.

Reference

Anderson, J.D., 2011. Fundamentals of Aerodynamics. New York.
Berg, J.J., 2015. Simulating water vapor plumes on Europa. Aerospace Engineering. University of Texas at Austin, Austin, TX, USA.
Berg, J.J., Goldstein, D.B., Varghese, P.L., Trafton, L.M., 2016. DSMC simulation of Europa water vapor plumes. Icarus 277, 370–380.
Bird, G.A., 1994. Molecular Gas Dynamics and the Direction Simulation of Gas Flows. Clarendon Press, Oxford, UK.
Burger, M.H., Sittler, E.C., Johnson, R.E., Smith, H.T., Tucker, O.J., Shematovich, V.I., 2007. Understanding the escape of water from Enceladus. J. Geophys. Res. 112.
Dettleff, G., 1991. Plume flow and plume impingement in space technology. Prog. Aerosp. Sci. 28, 1–71.
Dong, Y., Hill, T.W., Teolis, B.D., Magee, B.A., Waite, J.H., 2011. The water vapor plumes of Enceladus. J. Geophys. Res. 116.
Draper, J.S., Hill, J.A.F., 1966. Analytical approximation for the flow from a nozzle into a vacuum. J. Spacecraft Rockets 3, 1552–1554.
Esposito, L.W., et al., 2004. The Cassini ultraviolet imaging spectrograph investigation. Space Sci. Rev. 115, 299–361.
Goguen, J.D., et al., 2013. The temperature and width of an active fissure on Enceladus measured with Cassini VIMS during the 14 April 2012 South Pole flyover. Icarus 226, 1128–1137.
Hansen, C.J., et al., 2006. Enceladus' water vapor plume. Science 311, 1422–1425.
Hansen, C.J., et al., 2008. Water vapour jets inside the plume of gas leaving Enceladus. Nature 456, 477.
Hansen, C.J., et al., 2011. The composition and structure of the Enceladus plume. Geophys. Res. Lett. 38.
Hedman, M.M., et al., 2018. Spatial variations in the dust-to-gas ratio of Enceladus' plume. Icarus 305, 123–138.
Howett, C.J.A., Spencer, J.R., Pearl, J., Segura, M., 2011. High heat flow from Enceladus' south polar region measured using 10–600 cm−1 Cassini/CIRS data. J. Geophys. Res. 116 n/a-n/a.
Ingersoll, A.P., Ewald, S.P., 2011. Total particulate mass in Enceladus plumes and mass of Saturn's E ring inferred from Cassini ISS images. Icarus 216, 492–506.
Kasprzak, W.T., et al., 1996. Cassini orbiter ion neutral mass spectrometer instrument. In: Proc. Soc. Photo-Optical Instrumentation Engineers (SPIE). 2803. pp. 129–140.
Kieffer, S.W., Lu, X., Bethke, C.M., Spencer, J.R., Marshak, S., Navrotsky, A., 2006. A Clathrate Reservoir Hypothesis for Enceladus' South Polar Plume. Science 314, 1764–1766.
Kite, E.S., Rubin, A.M., 2016. Sustained eruptions on Enceladus explained by turbulent dissipation in tiger stripes. Proc. Natl Acad. Sci. 113, 3972–3975.
Porco, C., Nino, D.D., Nimmo, F., 2014. How the geysers, tidal stresses, and thermal emission across the south polar terrain of Enceladus are related. Astron. J. 148.
Porco, C.C., et al., 2006. Cassini observes the active south pole of Enceladus. Science 311, 1393–1401.

Porco, C.C., et al., 2004. Cassini imaging science: instrument characteristics and anticipated scientific investigations at Saturn. Space Sci. Rev. 115, 363–497.
Portyankina, G., Esposito, L.W., Ali, A., Hansen, C.J., 2016. Modeling of the Enceladus water vapor jets for interpreting UVIS star and solar occultation observations. In: Lunar and Planetary Science Conference. Woodlands, Texas, USA. pp. 2600.
Postberg, F., et al., 2009. Sodium salts in E-ring ice grains from an ocean below the surface of Enceladus. Nature 459, 1098.
Quick, L.C., Barnouin, O.S., Prockter, L.M., Patterson, G.W., 2013. Constraints on the detection of cryovolcanic plumes on Europa. Planet. Space Sci. 86, 1–9.
Saur, J., et al., 2008. Evidence for temporal variability of Enceladus' gas jets: modeling of cassini observations. J. Geophys. Res. 35.
Schmidt, J., Brilliantov, N., Spahn, F., Kempf, S., 2008a. Slow dust in Enceladus' plume from condensation and wall collisions in tiger stripe fractures. Nature 451, 685.
Schmidt, J., Brilliantov, N., Spahn, F., Kempf, S., 2008b. Slow dust in Enceladus' plume from condensation and wall collisions in tiger stripe fractures. Nature 451, 685.
Smith, H.T., Johnson, R.E., Perry, M.E., Mitchell, D.G., McNutt, R.L., Young, D.T., 2010. Enceladus plume variability and the neutral gas densities in Saturn's magnetosphere. J. Geophys. Res. 115.
Spencer, J.R., et al., 2006. Cassini encounters Enceladus: background and the discovery of a south polar hot spot. Science 311, 1401–1405.
Spitale, J.N., Hurford, T.A., Rhoden, A.R., Berkson, E.E., Platts, S.S., 2015. Curtain eruptions from Enceladus' south-polar terrain. Nature 521, 57.
Srama, R., et al., 2004. The Cassini cosmic dust analyzer. Space Sci. Rev. 114, 465–518.
Tenishev, V., Combi, M.R., Teolis, B.D., Waite, J.H., 2010. An approach to numerical simulation of the gas distribution in the atmosphere of Enceladus. J. Geophys. Res. 115.
Tenishev, V., Öztürk, D.C.S., Combi, M.R., Rubin, M., Waite, J.H., Perry, M., 2014. Effect of the tiger stripes on the water vapor distribution in Enceladus' exosphere. J. Geophys. Res. Planets 119, 2658–2667.
Teolis, B.D., et al., 2017. Enceladus plume structure and time variability: comparison of Cassini observations. Astrobiology 17, 926–940.
Teolis, B.D., Perry, M.E., Magee, B.A., Westlake, J., Waite, J.H., 2010. Detection and measurement of ice grains and gas distribution in the Enceladus plume by Cassini's ion neutral mass spectrometer. J. Geophys. Res. 115.
Tian, F., Stewart, A.I.F., Toon, O.B., Larsen, K.W., Esposito, L.W., 2007. Monte Carlo simulations of the water vapor plumes on Enceladus. Icarus 188, 154–161.
Waite, J.H., et al., 2006. Cassini ion and neutral mass spectrometer: Enceladus plume composition and structure. Science 311, 1419–1422.
Yeoh, S.K., Chapman, T.A., Goldstein, D.B., Varghese, P.L., Trafton, L.M., 2015. On understanding the physics of the Enceladus south polar plume via numerical simulation. Icarus 253, 205–222.
Yeoh, S.K., Li, Z., Goldstein, D.B., Varghese, P.L., Levin, D.A., Trafton, L.M., 2017. Constraining the Enceladus plume using numerical simulation and Cassini data. Icarus 281, 357–378.